Radial distribution of stars, gas and dust in SINGS galaxies: I. Surface photometry and morphology

J.C. Muñoz-Mateos[1], A. Gil de Paz[1], J. Zamorano[1], S. Boissier[2], D.A. Dale[3], P.G. Pérez-González[1], J. Gallego[1], B.F. Madore[4], G. Bendo[5], A. Boselli[2], V. Buat[2], D. Calzetti[6], J. Moustakas[7], R. C. Kennicutt, Jr.[8,9]

ABSTRACT

We present ultraviolet through far-infrared surface brightness profiles for the 75 galaxies in the *Spitzer* Infrared Nearby Galaxies Survey (SINGS). The imagery used to measure the profiles includes GALEX UV data, optical images from KPNO, CTIO and SDSS, near-IR data from 2MASS, and mid- and far-infrared images from *Spitzer*. Along with the radial profiles, we also provide multi-wavelength asymptotic magnitudes and several non-parametric indicators of galaxy morphology: the concentration index (C_{42}), the asymmetry (A), the Gini coefficient (G) and the normalized second-order moment of the brightest 20% of the galaxy's flux ($\overline{M}_{20}$). In this paper, the first of a series, we describe the technical aspects regarding the surface photometry, and present a basic analysis of the global and structural properties of the SINGS galaxies at different wavelengths. The homogeneity in the acquisition, reduction, and analysis of the

[1]Departamento de Astrofísica y CC. de la Atmósfera, Universidad Complutense de Madrid, Avda. de la Complutense, s/n, E-28040 Madrid, Spain; jcmunoz, agpaz, jaz, pgperez, jgm@astrax.fis.ucm.es

[2]Laboratoire d'Astrophysique de Marseille, OAMP, Université Aix-Marseille & CNRS UMR 6110, 38 rue Frédéric Joliot-Curie, 13388 Marseille cedex 13, France; samuel.boissier, alessandro.boselli, veronique.buat@oamp.fr

[3]Department of Physics and Astronomy, University of Wyoming, Laramie, WY; ddale@uwyo.edu

[4]Observatories of the Carnegie Institution of Washington, 813 Santa Barbara Street, Pasadena, CA 91101; barry@ociw.edu

[5]Astrophysics Group, Imperial College, Blackett Laboratory, Prince Consort Road, London SW7 2AZ; g.bendo@imperial.ac.uk

[6]Department of Astronomy, University of Massachusetts, Amherst, MA 01003; calzetti@astro.umass.edu

[7]Department of Physics, New York University, 4 Washington Place, New York, NY 10003, USA

[8]Institute of Astronomy, University of Cambridge, Madingley Road, Cambridge CB3 0HA, UK

[9]Steward Observatory, University of Arizona, Tucson, AZ 85721

results presented here makes of these data ideal for multiple unanticipated studies on the radial distribution of the properties of stars, dust, and gas in galaxies. Our radial profiles show a wide range of morphologies and multiple components (bulges, exponential disks, inner and outer disk truncations, etc.) that vary not only from galaxy to galaxy but also with wavelength for a given object. In the optical and near-IR, the SINGS galaxies occupy the same regions in the C_{42}-A-G-$\overline{M}_{20}$ parameter space as other normal galaxies in previous studies. However, they appear much less centrally concentrated, more asymmetric and with larger values of G when viewed in the UV (due to star-forming clumps scattered across the disk) and in the mid-IR (due to the emission of Polycyclic Aromatic Hydrocarbons at $8.0\,\mu$m and very hot dust at $24\,\mu$m). In the accompanying paper (Muñoz-Mateos et al. 2009) we focus on the the radial distribution of dust properties in the SINGS galaxies, providing a detailed analysis of the radial variation of the attenuation, the dust column density, the dust-to-gas ratio, the abundance of PAHs and the intensity of the heating starlight.

Subject headings: galaxies: photometry — galaxies: fundamental parameters — galaxies: structure — atlases

1. Introduction

Understanding the physical mechanisms that have shaped galaxies into their present-day forms has been one of the foremost goals in extragalactic astronomy. The current spatial distribution of stars, dust and gas results from the joint action of different processes, such as radially-varying gas-infall rate, star formation induced by spiral waves, the injection of metals in the interstellar medium, and secular re-arrangement of material within the disks, among others. In this regard, surface photometry has proven to be a convenient way to classify and analyze the radial structure of galaxies.

Radial profiles constitute an important observational constraint on the predictions of theoretical models of galaxy formation and evolution. Despite being a long-known empirical fact, the exponential nature of spiral disks still eludes a definitive explanation. Disk galaxies are supposed to form when baryons cool inside dark matter halos that have formed through gravitational instability, having initially acquired angular momentum from cosmological torques (Fall & Efstathiou 1980). Some authors appeal to conservation of angular momentum during the collapse as the origin of exponential disks (see e.g. Governato et al. 2007 and references therein). Others ascribe it to secular processes, such as viscosity-driven redistribution of angular momentum within the disks (Yoshii & Sommer-Larsen 1989; Fer-

guson & Clarke 2001).

To further complicate this issue, van der Kruit (1979) showed that the outer regions of spirals usually deviate from the inner exponential profile. Indeed, we now know that purely exponential profiles seem to be rather scarce. According to Pohlen & Trujillo (2006), only 10% of nearby spirals exhibit single exponential profiles lacking any evident change of slope[1] (the so-called type I profiles). Most disks, roughly 60%, have an inner exponential profile followed by an steeper outer one (type II), and the remaining 30% have a shallower outer exponential (type III). Several mechanisms have been proposed to explain downward-bending profiles, ranging from angular momentum cutoffs to a threshold for star formation (see Pohlen at al. 2008 for a recent review on the subject).

Surface photometry in the ultraviolet, which traces recent ($\lesssim 1\,\mathrm{Gyr}$) star formation, has also led to new and surprising observational tests of our understanding of disk evolution. The discovery of extended UV (XUV) emission in the outskirts of many spirals (Thilker et al. 2005, 2007; Gil de Paz et al. 2005) provides a first-hand view of present-day disk growth and assembly. UV profiles can be combined with mid- and far-infrared ones to derive the radial variation of dust attenuation in spirals (Boissier et al. 2004, 2005, 2007). Since both stars and dust contribute to the observed color gradients in galaxies (de Jong 1996; MacArthur et al. 2004), these extinction profiles are key to disentangling the two effects, and thereby to interpret broadband color gradients in terms of radial changes in the mean age of the stellar populations (Muñoz-Mateos et al. 2007). Furthermore, when compared with gas profiles, one can derive the radial variation of the dust-to-gas radio, which is also expected to depend on the star formation history at different radii (Boissier et al. 2004). Besides, radial profiles can be also used to constrain the mathematical form of the star formation law (Wong & Blitz 2002; Heyer et al. 2004; Boissier et al. 2007; Thilker et al. 2007).

Light profiles have also played an important role when quantifying the morphology of galaxies. Ever since spirals were identified as having a bulge and an exponential disk with different light profiles (de Vaucouleurs 1958; Freeman 1970), bulge-disk decompositions and Sérsic-profile fitting (Sérsic 1968) have been routinely used to quantify galaxy morphology. However, the applicability of these methods can be hampered by the presence of bars, compact nuclei, bright spiral arms or disk truncations, or when observing at wavelengths tracing recent star formation.

---

[1] This is often referred to as a 'break' or 'truncation'. This can be misleading, as it suggests a sudden cutoff in the emission, while it is just a change of slope. However, since it has become a convention, throughout this paper we will use 'truncated' and 'anti-truncated' as synonyms of 'down-bending' and 'up-bending', respectively.

Non-parametric morphology estimators differ from the B/D ratio or the Sérsic index in that they do not implicitly assume a functional form for the spatial distribution of light in galaxies. The concentration index (de Vaucouleurs 1977; Kent 1985) and the rotational asymmetry (Schade et al. 1995) are the most extensively used parameters of this kind in the literature (Abraham et al. 1996a, 1996b; Bershady et al. 2000; Kuchinski et al. 2000, 2001; Conselice et al. 2000; Taylor-Mager et al. 2007). More recently, the toolbox of non-parametric morphology estimators has been upgraded with the incorporation of new indicators. The Gini coefficient (G, Abraham et al. 2003) measures the relative contribution of bright and faint pixels to the total galaxy luminosity. The normalized second-order moment of the pixels constituting the brightest 20% of the galaxy flux ($\overline{M}_{20}$, Lotz et al. 2004) is closely related to classical concentration indices, but it is more weighted by the spatial distribution of bright off-center regions.

It follows from the discussion above that a complete description of the morphology of galaxies across a wide wavelength range is paramount for our understanding of galaxy buildup. This is the first paper in a series aiming to characterize the radial distribution of stars, dust and gas in nearby galaxies, making use of the multi-wavelength data sets available for the galaxies in the *Spitzer* Infrared Nearby Galaxies Survey (SINGS; Kennicutt et al. 2003). Here we present surface brightness radial profiles ranging from the far-ultraviolet to the far-infrared, along with asymptotic magnitudes and the aforementioned non-parametric morphology estimators. In the accompanying paper (Muñoz-Mateos et al. 2009, Paper II hereafter), we carry out a thorough study of the radial distribution of several dust properties: attenuation, surface density, PAH abundance, heating starlight intensity and dust-to-gas ratio. Finally, we are also fitting our radial profiles with models for the chemical and spectro-photometric evolution of spirals of Boissier & Prantzos (2000), to infer the radial change of the SFH in a self-consistent frame. The results of this study will be presented in a forthcoming paper. In addition to the analysis of the basic global and structural parameters of the SINGS sample, the data presented here possess an important legacy value for future studies of galactic structure.

This paper is organized as follows. In Section 2 we outline the characteristics of the galaxy sample and the multi-wavelength imagery. Section 3 details the technical aspects of the analysis, such as removing foreground and background objects in the original images, obtaining the radial profiles and measuring the morphological estimators. The results are discussed in Section 4, and our main conclusions are finally summarized in Section 5. In Appendix A we explain the corrections applied to the zero-points of some of the optical images.

2. The sample and data

The SINGS sample (Kennicutt et al. 2003) consists of 75 nearby galaxies selected to cover the range in morphological type, luminosity and FIR/optical luminosity observed in the local universe. Moreover, the SINGS galaxies also span a reasonably wide range in additional properties, such as nuclear activity, spiral and bar structure, inclination, surface brightness and environment. It lacks, however, any significant luminous or ultra-luminous infrared galaxy (i.e. with $L_{\mathrm{IR}} > 10^{11}\,\mathrm{L}_\odot$). All galaxies are closer than 30 Mpc, with the median distance being 10 Mpc. Note, however, that early-type galaxies (E, S0 and Sa-Sab) tend to be further away than the bulk of the sample, while irregulars are usually much closer. In spite of being neither a flux- nor a volume-limited sample (and thus lacking statistical power as a whole), this sample constitutes an excellent benchmark to study the interplay between star formation and the ISM in environments with a large variety of physical properties. The main properties of the SINGS galaxies are summarized in Table 1.

Throughout the remainder of this paper we quote all the multi-wavelength data in the AB magnitude system, otherwise mentioned. The AB magnitudes can be translated into flux densities following the definition of Oke (1974):

$$m_{\mathrm{AB}}(\mathrm{mag}) = -2.5\log F_\nu(\mathrm{Jy}) + 8.9 \tag{1}$$

2.1. GALEX data

The GALEX mission (Martin et al. 2005) has observed nearly all SINGS galaxies in the FUV ($\lambda_{eff} = 151.6\,\mathrm{nm}$) and the NUV ($\lambda_{eff} = 226.7\,\mathrm{nm}$). A dichroic beam splitter allows these observations to be carried out simultaneously at both bands, although only NUV data are available for a few galaxies, since the FUV detector had to be occasionally turned off for safety reasons. Photon lists are created from individual photon detections, and are then translated into intensity maps, with a final pixel-scale of $1.5''$. The flux calibration is based on white dwarf standard stars, with an estimated uncertainty of 0.15 mag at both wavelengths for the pipeline version used here (the same as in Gil de Paz et al. 2007).

The size of the PSF varies slightly with the position on the detector and the brightness of the source, but the FWHM is typically $6''$, which corresponds to a spatial scale of $\sim$300 pc at the median distance of the SINGS sample. The GALEX resolution nicely matches that of the MIPS $24\,\mu$m band, although the PSFs are different, the Airy rings being noticeable only in the $24\,\mu$m data.

2.2. Optical data

Optical images for the SINGS galaxies were taken at the Kitt Peak National Observatory (KPNO) 2.1 m telescope and the Cerro Tololo Inter-American Observatory (CTIO) 1.5 m telescope, using Harris $BVRI$ filters. The raw frames have pixel scales of $0.305''$ and $0.433''$ for the KPNO and CTIO telescopes, respectively, and were processed following standard reduction routines for optical images. These include bias subtraction, flat-field correction, cosmic-ray removal and mosaicking for those galaxies larger than the instrument's field of view ($10'$ at KPNO and $14.5'$ at CTIO).

The images were flux-calibrated with photometric standard stars imaged during each observing run. However, the final frames exhibit non-negligible zero-points offsets −compared to the global shape of the SED− whose origin is difficult to trace back and has not been fully elucidated. In order to deal with this problem, we initially searched for all publicly available optical images for the SINGS galaxies using NED. After closely examining the retrieved data, we soon realized that the data quality was quite heterogeneous in terms of spatial coverage, image depth and spatial resolution.

We finally opted for using images from the Sloan Digital Sky Survey (SDSS; York et al. 2000) for as many galaxies as possible. We relied on imagery from the Data Release 6 (Adelman-McCarthy et al. 2008). The necessary frames for each galaxy were downloaded and mosaicked together. The conversion from counts to physical units was carried out following the prescriptions provided in the SDSS DR6 Flux Calibration Guide[2], using the calibration factors of the frame that was used as a flux reference when building each mosaic. Surface brightness profiles were then measured on these images as explained in Section 3.2. Although absolute zero-point errors for the SDSS photometry have not been reported yet, the relative photometry is known to have a uniformity of 2%-3%.

Despite their short exposure time (54 seconds), we found the SDSS data to be surprisingly useful for measuring the profiles of the outer regions of the galaxies. Since they are taken in drift-scan mode, they exhibit an almost flat background, thus matching the quality of images taken with similar telescopes but larger exposure times (see also Erwin et al. 2008 in this regard).

For those galaxies not in the SDSS, we opted for recalibrating their SINGS optical images using the extensive catalog of aperture photometry compiled in Prugniel & Heraudeau (1998). The recalibration procedure is described in detail in Appendix A. We estimate that the zero-point error of our final recalibrated data is 10%-15%.

---

[2]http://www.sdss.org/dr6/algorithms/fluxcal.html

In Table 1 we indicate which approach was chosen for each particular galaxy, namely: to measure the profiles on the SDSS data (32 galaxies) or to recalibrate the original SINGS images with the catalog of Prugniel & Heraudeau (1998) (23 galaxies). The remaining 20 objects (mostly irregular galaxies) were not included in this catalog or, if they were, the resulting recalibrated optical points did not look reliable enough when compared to the adjacent photometric data-points.

It should be noted that these zero-point issues do not affect the non-parametric morphological estimators. These structural parameters were thus measured on both the SDSS and the SINGS images, regardless of whether the latter had been recalibrated or not.

We do not provide neither photometry nor structural parameters in the very few cases when significant patches of the galaxy are missing from the mosaics (as happens, for instance, in the R-band image of NGC 3031).

2.3. 2MASS data

Since the SINGS galaxies are too large to fit into a single 2MASS scan, the corresponding mosaics were retrieved from the 2MASS Large Galaxy Atlas (LGA; Jarrett et al. 2003). The reader is referred to that paper for an in-depth description of the LGA data. The images have a pixel-scale of $1''$, and a PSF FWHM of $2'' - 3''$, depending on the seeing conditions (120 pc at the median distance of 10 Mpc). The calibration errors are estimated to be 0.011, 0.007 and 0.007 mag in J, H and K_S, respectively (Cutri et al. 2003). The Vega-based magnitudes of 2MASS were converted into the AB system by applying the zero-point corrections quoted in Cohen et al. (2003):

$$
\begin{aligned}
J_{\mathrm{AB}} &= J_{\mathrm{Vega}} + 0.894 \\
H_{\mathrm{AB}} &= H_{\mathrm{Vega}} + 1.374 \\
K_{\mathrm{S\ AB}} &= K_{\mathrm{S\ Vega}} + 1.840
\end{aligned}
\tag{2}
$$

2.4. Spitzer data

Mid-infrared images at 3.6, 4.5, 5.8 and $8.0\,\mu$m were obtained using the Infrared Array Camera (IRAC, Fazio et al. 2004) onboard *Spitzer* (Werner et al. 2004). The FWHM of the PSF at each channel are $1.7''$, $1.7''$, $1.9''$ and $2.0''$ respectively, probing physical scales of 80-100 pc at the median distance of the sample. Mosaics were taken for galaxies larger than IRAC's field of view ($\sim 5'$), while the smaller ones were observed in a single dither pattern.

The images provided in the SINGS Fourth Data Delivery are based on the Version 13 Basic Calibrated Data produced by the *Spitzer* Science Center. They have undergone additional processing to account for geometrical distortion and rotation, residual bias structure, image offsets, bias drift, cosmic ray removal and constant background subtraction, as well as photometric calibration. The final pixel scale is set to $0.75''$. Although the estimated zero-point error is $\sim 2\%$ (Reach et al. 2005), the uncertainty in the aperture corrections increase the global error up to $\sim 10\%$ [3]. These corrections account for the diffuse scattering of incoming photons throughout the IRAC array, and must be applied even for large apertures, since the photometry is normalized to finite apertures of $12''$, rather than infinite ones.

The Multi-band Imaging Photometer (MIPS, Rieke et al. 2004) was used to image the galaxies at 24, 70 and 160μm, with FWHM of $5.7''$, $16''$ and $38''$, respectively. These resolutions correspond to physical scales of 0.28, 0.78 and $1.84\,$kpc at the median distance of the sample. The observations were carried out using the scan-mapping mode, visiting each galaxy in separate epochs and with different orientations to identify asteroids and remove detector artifacts at the two longer wavelengths. Further processing by the SINGS team include conversion of 70 and $160\,\mu$m signal ramps to slopes, flat-fielding, subtraction of zodiacal light at $24\,\mu$m, removal of short-term variations in the signal due to drift, background subtraction, final mosaicking and calibration. The delivered frames at 24, 70 and $160\,\mu$m have pixel-scales of $1.5''$, $4.5''$ and $9.0''$, respectively, chosen to be integer multiples of that of the IRAC mosaics, while still properly sampling the MIPS PSF. The estimated calibration errors at each band are 4%, 5% and 12%, respectively (Engelbracht et al. 2007; Gordon et al. 2007; Stansberry et al. 2007).

3. Analysis

3.1. Object masking

Masking the brightest field stars and background galaxies is essential to obtain good quality surface brightness profiles. In order to detect these sources, we run SExtractor (Bertin & Arnouts 1996) in dual mode on the IRAC images using the $3.6\,\mu$m one as the detection image. Although SExtractor is mainly oriented towards source-detection in large-scale galaxy surveys, the configuration parameters can be tuned so that it can also deblend and extract sources embedded within the light of nearby galaxies. Note that we only use the results from SExtractor to identify and mask foreground stars and background galaxies.

---

[3]http://ssc.spitzer.caltech.edu/irac/calib/extcal/

For each detected source, SExtractor yields a stellarity index (`CLASS_STAR`) ranging from 0 for extended sources to 1 for point-like ones. Following the methodology described in Robin et al. (2007), we concluded that `CLASS_STAR` = 0.8 provides a sufficiently clean separation between resolved and unresolved sources. Objects with $f_{3.6\mu m} > f_{5.8\mu m}$ and `CLASS_STAR` $\geq$ 0.8 are automatically classified as foreground stars. A visual inspection confirms that these two simple criteria are quite effective at masking most of them. In some galaxies where individual stars might be seen (especially in the outer regions), an additional criterion is added to avoid excessive masking in these areas. We define a 'contrast parameter' $\Gamma = |f_{\mathrm{global}} - f_{\mathrm{local}}|/f_{\mathrm{global}}$, where f_{local} is the $3.6\,\mu m$ flux density computed after having subtracted a local background[4] and f_{global} is obtained assuming a constant background value all over the image, the same for all sources. In other words, Γ is a quantitative measure of how bright is a given source compared to its surroundings. By tuning Γ we can control to what extent doubtful sources embedded in the galaxy light are masked or not. We found that sources with $\Gamma < 0.2$ are usually too contaminated by galaxy light to allow for a proper classification. This is not a concern, anyway, for these sources are too faint to affect our radial profiles, asymptotic magnitudes and morphological parameters.

As for extended objects (i.e. those with `CLASS_STAR` < 0.8), they can be either local HII regions belonging to the nearby galaxy or entire background galaxies. The former can be easily identified thanks to the fact that the ratio of the emission at 5.8 and 8.0 μm due to PAHs holds rather constant in the diffuse ISM of nearby galaxies (Draine & Li 2007). This is clearly seen in Fig. 1, where we plot an IRAC color-color diagram for all the sources detected in the IRAC images of NGC 6946. Star-forming regions belonging to NGC 6946 are arranged in a very thin cloud with an almost constant $(5.8\mu m - 8.0\mu m)$ color, while background galaxies lie outside this region, because they are either redshifted spirals or ellipticals. After several trials, we found that most local HII regions in our galaxies can be isolated by means of the following color criteria:

$$F_{5.8\mu m}/F_{8.0\mu m} \quad > \quad 0.25 \tag{3}$$
$$F_{5.8\mu m}/F_{8.0\mu m} \quad < \quad 0.63 \tag{4}$$
$$F_{3.6\mu m}/F_{5.8\mu m} \quad < \quad 1.58 \tag{5}$$

These criteria, combined with SExtractor's stellarity index and a contrast parameter similar to the one described above for stars, perform rather well for the majority of galaxies

---

[4]SExtractor applies a median filter in boxes with a user-defined width (15 pixels in our case), and then performs a bi-cubic spline interpolation to produce a background map. We opted to use this as the local background when doing the photometry, instead of measuring it within a certain ring around each source, since we are interested in removing the smooth emission arising from the galaxy.

in the SINGS sample. It should be noted that the $5.8\,\mu$m and $8.0\,\mu$m bands may be highly contaminated by stellar emission in the central regions of galaxies with large bulges. Indeed, we checked that some sources in these regions failed the color criteria, but they were not masked thanks to the contrast parameter. Otherwise, they would have been misclassified as background ellipticals.

This technique was just used to automatically generate masks which were then visually inspected to detect possible errors; in the few cases when it was needed, we unmasked regions of the galaxy that had been misclassified as field objects, or masked sources that had eluded the detection and classification process. These masks were then applied to all images at every wavelength and, for each one of them, artifacts such as bleeding, reflections and diffraction spikes were also cleaned out. As an example, in Fig. 2 we show the original $3.6\,\mu$m image of NGC 6946 and the one resulting after the cleaning process.

By no means is this detection and classification procedure intended to be accurate at the level of individual sources. Rather, it simply allows us to mask the most relevant objects that could contaminate the emission from the nearby galaxy when measuring the profiles.

3.2.   Surface photometry

We have worked with two sets of radial profiles: high resolution profiles for all data between the FUV and $24\,\mu$m, with a radial step of $6''$ (matching the GALEX and MIPS $24\,\mu$m FWHM) and lower resolution ones with a radial increment of $12''$ at 70 and 160μm. While the latter actually oversample the MIPS PSF at those bands, such a radial step is desirable to properly measure the asymptotic magnitudes. In Paper II we present $48''$-resolution profiles measured on GALEX, IRAC and MIPS images, spatially degraded in order to match the size and shape of their PSFs to that of the 160μm channel. These profiles are used to determine the radial variation of several dust properties and are also combined with HI profiles from The HI Nearby Galaxies Survey (THINGS; Walter et al. 2008) and CO profiles from the literature, to study the radial variation of the dust-to-gas ratio.

Surface brightness profiles in GALEX FUV and NUV bands were presented by Gil de Paz et al. (2007); 2MASS K-band profiles for 16 out of the 75 SINGS galaxies were included in the sample studied by Muñoz-Mateos et al. (2007). The profiles presented here were obtained in the same way as was done for the GALEX and 2MASS images in those papers. We used IRAF[5] task ELLIPSE to measure the mean intensity along elliptical isophotes with fixed ellipticity and position angle, equal to those of the $\mu_B = 25$ mag arcsec^{-2} isophote from the RC3 catalog[6] (de Vaucouleurs et al. 1991). For those galaxies for which these

geometrical parameters were not quoted in the RC3 catalog, we used the values provided in NED. The center of these ellipses were set at the coordinates shown in Table 1, with constant increments of $6''$ and $12''$ along the semimajor axis to a final radius at least 1.5 times the D25 diameter. This value was increased if significant emission was seen beyond that radius (especially in the UV bands). In order to measure the different fluxes in the same regions of each galaxy, the same set of elliptical isophotes was used in all bands.

In order to derive the uncertainties in the surface brightness profiles, we followed the methodology described in Gil de Paz & Madore (2005). The following expression relates the intensity in counts per pixel (I) with the surface brightness in $\mathrm{mag\,arcsec}^{-2}$ (μ):

$$\mu = C - 2.5\log(I - I_{\mathrm{sky}}) + 5\log(\mathrm{arcsec\,pixel}^{-1}) \qquad (6)$$

where C is the corresponding zero-point constant. To first order, the error in μ can be obtained as:

$$\Delta\mu = \sqrt{(\Delta C)^2 + \left(\frac{2.5\log(e)}{I - I_{\mathrm{sky}}}\right)^2 (\Delta I^2 + \Delta I_{\mathrm{sky}}^2)} \qquad (7)$$

The uncertainty in the incident flux per pixel can be estimated assuming poissonian statistics:

$$\Delta I = \sqrt{\frac{I}{g_{\mathrm{eff}} N_{\mathrm{isophote}}}} \qquad (8)$$

where g_{eff} is the effective gain, necessary to convert the incoming flux per pixel I into electrons, and N_{isophote} is the number of pixels used to compute the mean surface brightness within each isophote. In general, a single value of g_{eff} was used for all the pixels in each frame. However, each IRAC image has an associated weight-map indicating the coverage of each pixel by the different pointings of the corresponding mosaic. Therefore, for the IRAC frames a spatially varying effective gain was derived from these weight-maps.

Our approach differs from that of Gil de Paz & Madore (2005) in the sense that these authors rely on the *rms* along each isophote to estimate the error on I. Therefore, besides statistical uncertainties their errorbars also include spatial variations in the flux coming from different regions. Since our data-set spans a very wide range of wavelengths, the *rms* within

---

[5]IRAF is distributed by the National Optical Astronomy Observatories, which are operated by the Association of Universities for Research in Astronomy, Inc., under cooperative agreement with the National Science Foundation.

[6]Except for NGC 5194, whose original values were highly affected by its companion galaxy, NGC 5195. Our finally adopted values better match the actual shape of NGC 5194 itself.

each isophote can vary due to the different degree of clumpiness of stars (old and young), dust and gas. Also, in those bands where the PSF FWHM is significantly larger than the actual size of the physical structures being probed (e.g. at the longest MIPS wavelengths), the measured rms could be artificially smoothed. Therefore, we prefer to consider only the purely statistical error in the mean surface density within each isophote.

As for the uncertainty in the sky level, it essentially comes from two sources: high and low spatial frequency errors. The former results from the combination of Poisson noise in $I_{\rm sky}$ plus pixel-to-pixel flat-fielding errors. The latter is due to large-scale flat-fielding errors (because of residual gradients, reflections, etc.) as well as real background structures such as cirrus. In order to quantify these two sources of uncertainty, for each frame we measured the sky in ~ 20 square regions of $N_{\rm region}$ pixels each, randomly placed around each galaxy far enough from it to avoid contamination from the galaxy itself. $I_{\rm sky}$ was then determined as the mean sky value in all boxes. We also computed the mean standard deviation, $\langle\sigma_{\rm sky}\rangle$, and the standard deviation of the mean sky values among different boxes, $\sigma_{\langle{\rm sky}\rangle}$. Thus,

$$\Delta I_{\rm sky} = \sqrt{\frac{\langle\sigma_{\rm sky}\rangle^2}{N_{\rm isophote}} + \max\left(\sigma_{\langle{\rm sky}\rangle}^2 - \frac{\langle\sigma_{\rm sky}\rangle^2}{N_{\rm region}}, 0\right)} \qquad (9)$$

The second term accounts for the large-scale background errors, and might be especially important in the outer regions of the galaxy, where we average the flux along widely separated regions of the detector. Even in a frame with a perfectly flat background the measured large-scale variance $\sigma_{\langle{\rm sky}\rangle}^2$ would be nonzero. If no large-scale variations were present and we placed several sky boxes with only one pixel each ($N_{\rm region} = 1$), then the measured large-scale variance would be equal to the local one, $\langle\sigma_{\rm sky}\rangle^2$. In general, $\langle\sigma_{\rm sky}\rangle^2/N_{\rm region}$ is the expected value of $\sigma_{\langle{\rm sky}\rangle}^2$ in the absence of true background variations across the frame. Therefore, the difference between both quantities reflects the contribution of actual large-scale background changes to the final error. When such a difference is negative −something that can statistically happen− we assume that large-scale variations are not present.

The technique described in this section could not be fully applied to the 70μm and 160μm images given their small size. Since we could not fully guarantee that our sky boxes did not overlap with the faintest isophotes of the galaxy, in these cases we relied on the sky values and errors included in the FITS headers of each image, which were obtained from larger mosaics.

The resulting profiles are shown in Tables 2, 3 and 4. The quoted errors in the surface photometry do not include zero-point errors, which must be considered when comparing fluxes measured in different bands. The typical zero-point uncertainties for each band can be found in the corresponding subsection within Section 2. Also, note that the large errors in the

outer regions of most profiles are usually dominated by large-scale errors in the background determination. In many cases there is emission from the galaxy that clearly emerges above the local noise, so the large associated uncertainties do not necessarily imply non-detections.

The radial profiles were corrected for Galactic extinction as in Dale et al. (2007) using the color excesses from the maps of Schlegel et al. (1998) and the extinction curve of Li & Draine (2001), assuming $R_V = 3.1$.

While surface photometry with elliptical isophotes is a technique routinely used in the literature, there are some caveats worth mentioning. First of all, in moderately inclined galaxies with prominent bulges or halos, such as NGC 4594 (the Sombrero Galaxy), the shape of the RC3 ellipses is intermediate between that of the disk and the bulge. Disentangling these components usually requires more sophisticated procedures (see e.g. Bendo et al. 2006). More oblate ellipses do certainly fit the disk in the mid- and far-IR, where it is neatly detached from the surrounding structures. However, such ellipses still suffer from similar problems in the optical and UV, since they probe both the foreground half of the disk, which is heavily obscured by dust lanes, and the background half of the disk behind the bright bulge.

Secondly, a more general problem in all edge-on galaxies is that light from the outer disk might end up being contaminated by more central regions when performing the azimuthal average. Simply measuring the surface brightness along the major axis is not devoid of problems either, for the surface brightness at a given observed radius results from the combined emission of sources along the line of sight, located at very different physical distances from the center of the galaxy. Since the optical depth depends on wavelength, a full radiative transfer treatment is usually more suitable in these cases (see e.g. Xilouris et al. 1999; Popescu et al. 2000).

Finally, although irregulars may not necessarily exhibit a disk-like structure, radial profiles are still useful as a coarse measurement of the radial variation of their physical properties. In the case of elliptical galaxies it should be noted that profiles with elliptical isophotes cannot be interpreted in the same way as those of projected disks.

3.2.1. Corrections for the IRAC and MIPS data

The IRAC surface brightness profiles required being corrected for aperture effects to account for the diffuse scattering of incoming photons throughout the IRAC array[7]. While usual aperture corrections account for the extended wings of the PSF due to the diffraction of light through the telescope optics, the ones considered here correct for the diffraction of

light through the detector substrate (Reach et al. 2005).

In order to properly correct our radial profiles profiles, we first computed the growth curve, thus getting the accumulated flux up to each given radius. We then applied the proper extended source aperture corrections to each elliptical aperture, and then recomputed μ by subtracting the flux of adjacent apertures.

For the 70μm image, prior to measuring the profiles we applied the preliminary correction for nonlinearity effects quoted in Dale et al. (2007), which is derived from data presented by Gordon et al. (2007).

3.2.2. Asymptotic magnitudes

The asymptotic magnitudes —that is, the ones that would be obtained by measuring with a hypothetically infinite aperture— can be derived by means of the growth curve (see e.g. Cairós et al. 2001). The procedure is depicted in Fig. 3. We computed the radial gradient in the accumulated magnitude at each radius, which typically exhibits a linear behavior when plotted against the accumulated magnitude. We then applied a weighted linear fit to the points within a suitable outer spatial range, with the asymptotic magnitude being the y-intercept of this fit, that is, the extrapolation towards a zero gradient. The resulting values are shown in Tables 5, 6 and 7. The uncertainties were estimated with the classical statistical formulae, from the residual dispersion of the data points with respect to the fitting line. However, these errors do not include calibration uncertainties (see Section 2).

3.3. Non-parametric morphological estimators

3.3.1. Concentration indices.

From the growth curve at each wavelength, we computed the concentration indices C_{31} (de Vaucouleurs 1977) and C_{42} (Kent 1985), defined as:

$$C_{31} = \frac{r_{75}}{r_{25}} \tag{10}$$

$$C_{42} = 5\log\left(\frac{r_{80}}{r_{20}}\right) \tag{11}$$

---

[7]See http://ssc.spitzer.caltech.edu/irac/calib/extcal/

where r_x are the radii along the semi-major axis encompassing $x\%$ of the total flux of the galaxy at each band, the latter computed from the asymptotic magnitude. Note that since we are dealing with elliptical apertures, a correction for inclination needs not to be applied. For the remainder of the analysis presented here we will focus on C_{42} only, since both indices are tightly correlated[8].

The resulting values of C_{42} are quoted in Table 8. We have flagged as unreliable those values in which the inner radius r_{20} is smaller than the innermost point of our profiles ($6''$ at $24\,\mu$m and $12''$ at $70\,\mu$m and $160\,\mu$m, the latter two oversampling the PSF, see Section 3.2). In these cases the quoted values are then just lower limits. Taking into account the shape and spatial extent of the PSF is necessary in order not to over-interpret concentration indices in unresolved sources. This is specially critical in the MIPS bands, given the broad and strong Airy rings of the corresponding PSFs. We measured the concentration index C_{42} on model images of the MIPS PSFs, resulting in values of 3.7, 3.5 and 3.6 at $24\,\mu$m, $70\,\mu$m and $160\,\mu$m, respectively. We also found that $r_{20} \simeq 2'', 6''$ and $12''$ at those bands, which lie below or close to the smallest radius used in the galaxy profiles, so the corresponding values of C_{42} have been flagged when necessary as explained above.

Although when measuring C_{42} we rely on the centers given in the RC3 catalog, for the asymmetry and the second-order moment we follow an iterative process to find the center (see below). We have checked that offsets $\lesssim 3''$ have a negligible impact on C_{42}. In most cases the differences between the resulting values are just $\sim$0.01-0.001. Only in highly concentrated objects with small values of r_{20} do the discrepancies amount to $\sim$0.3-0.1.

3.3.2. Asymmetry.

Several mathematical definitions for computing the asymmetry can be found in the literature (Schade et al. 1995; Abraham et al. 1996b; Kuchinski et al. 2000, Conselice et al. 2000), although the philosophy behind all of them is essentially the same. It involves comparing the original image of a galaxy with its rotated counterpart, the rotation angle being usually 180° (although other angles can also yield useful information, see Conselice et al. 2000).

Here we adopt the definition of the asymmetry given by Abraham et al. (1996b):

$$A = \frac{1}{2}\left[\frac{\sum|I_{180°} - I_0|}{\sum|I_0|} - \frac{\sum|B_{180°} - B_0|}{\sum|I_0|}\right] \tag{12}$$

---

[8]The values of C_{31} can be obtained upon request from the first author.

I_0 and $I_{180°}$ are the intensities of the original and rotated images, respectively, and B_0 and $B_{180°}$ the intensities of background pixels and their rotationally-symmetric counterparts. The sum is carried out over all pixels within a certain aperture (see below). By taking the absolute value, the sky-noise introduces a certain positive signal in A that has to be subtracted in order to get the asymmetry of the galaxy itself. In principle this can be done by computing the asymmetry within a reasonably large patch of sky, free from emission coming from the galaxy (hence the second term in Eq. 12). However, this is not always possible in many images of our very extended sources, and it also tends to increase the computation time. Lauger et al. (2005) demonstrate that the noise asymmetry can be estimated by assuming poissonian statistics for the sky:

$$\sum \left| B_{180°} - B_0 \right| = \frac{2}{\sqrt{\pi}} \sigma_{\mathrm{sky}} N_{\mathrm{pix}} \qquad (13)$$

where σ_{sky} is the sky noise, measured as explained in Section 3.2, and N_{pix} is the number of pixels within the aperture used to derive the asymmetry in the galaxy. We verified that Eq. 13 is indeed valid for our images.

The asymmetry was measured within elliptical apertures with position angles, diameters and axis ratios equal to those of the $\mu_B = 25$ mag arcsec^{-2} isophotes from the RC3 or NED, and the resulting values are shown in Table 8. The use of isophotal radius is discouraged when comparing galaxies within large redshift intervals, since they might be affected by cosmological surface brightness dimming, k-correction, evolution and zero-point offsets. The use of the Petrosian η-function (Petrosian 1976) is usually more convenient in these cases (Bershady et al. 2000). It is defined as[9] $\eta(r) = I(r)/\langle I(r) \rangle$, i.e., the local surface brightness at a given radius r divided by the average surface brightness *inside* r. By definition, $\eta(r)$ is equal to 1 at $r = 0$ and approaches 0 at larger radii. The Petrosian radius r_P is such that $\eta(r_P)$ is equal to a certain value, usually 0.2. We found that the Petrosian radius often misses significant emission from the outer regions of many galaxies. Since the SINGS galaxies do not suffer from the cosmological issues listed above, the choice of employing the RC3 apertures is probably more justified in our case. While these apertures encompass more light than those derived from the η-function, they still miss some light of the very outer regions of the galaxies. Increasing the aperture size would introduce more sky in the less spatially-extended bands, thus making the subtraction of the noise asymmetry more critical. The choice of the RC3 ellipses constitutes a compromise solution; as long as A is computed consistently in all bands, the trends with wavelength should remain essentially correct.

In any case, for the sake of comparison we have also computed A within ellipses whose

---

[9]This is actually the inverted form of the original Petrosian function.

semi-major axis were set equal to the Petrosian radius, such that $\eta(r_P) = 0.2$ (see Table 1). Considering all bands together, we find that the difference between the asymmetries computed with both apertures is negligible, with $\langle A_{R25} - A_{r_P} \rangle = -0.005$ and a scatter of ± 0.009. This holds true on a band-by-band basis as well, except in those with poorer S/N ratios (like the u, z, J, H and K_S bands) where the offsets, while still smaller than the scatter, seem to be statistically significant. Those slight discrepancies are most likely due to the subtraction of the sky asymmetry being more delicate in those cases. Conselice et al. (2000) computed A both within r_P and $1.5r_P$ (incidentally, $R25 \sim 1.5r_P$ on average for the SINGS galaxies). We have checked from their published data that the difference between both cases is also negligible, with a scatter similar to ours.

The center of rotation was determined by minimizing the asymmetry. Starting from the central positions quoted in the RC3, we computed the asymmetry over a grid of (x, y) positions, recentering and repeating the process until a minimum value was found. To account for differences in the astrometrical calibration and resolution of the images, we allowed a maximum difference of $3''$ from the initial central coordinates. Objects requiring larger offsets are intrinsically asymmetric, the centers minimizing A probably not being the actual centers of the galaxy.

It should be noted that since A is computed on a pixel-by-pixel basis, the precise final values may depend on several parameters, such as the signal-to-noise ratio and the spatial resolution. Conselice et al. (2000) showed that A drops when one is unable to resolve structures smaller than $0.5\,\text{kpc}$, although for large galaxies asymmetries with a resolution of $\sim 1\,\text{kpc}$ may be still acceptable. Bendo et al. (2007) found that $A_{3.6\mu\text{m}}$ does not strongly depend on distance in the SINGS galaxies, but $A_{24\mu\text{m}}$ does, thus implying that other bands also showing inherently clumpy structures might be affected as well. We opt for a conservative approach and flag those values of A in which the spatial resolution at each particular band does not allow resolving structures smaller than $0.5\,\text{kpc}$. This mainly affects the $70\,\mu\text{m}$ and $160\,\mu\text{m}$ bands and, in galaxies further than $17\,\text{Mpc}$, the GALEX and $24\,\mu\text{m}$ images too.

The S/N ratio can also bias the derived values of A (Lotz et al. 2004; Lauger et al. 2005). All in all, an accurate determination of the asymmetry as a function of wavelength would require setting all images to a common PSF size, plate scale and depth, which is beyond the scope of this paper. Note, however, that differences in these parameters within the SINGS imagery are not that large anyway (except at $70\,\mu\text{m}$ and $160\,\mu\text{m}$ in terms of resolution, and also the 2MASS bands regarding the S/N ratio). The aforementioned corrections, therefore, are not as critical as when analyzing the morphology of galaxies in cosmological surveys (see e.g. López-Sanjuan et al. 2009 and references therein). Nevertheless, the results presented here should be treated cautiously, as our intention is simply to depict broad general trends.

3.3.3.   Gini coefficient.

The Gini coefficient (Gini 1912) is a statistical parameter widely used in econometrics to determine how wealth is distributed in a given population. It was adapted by Abraham et al. (2003) for galaxy morphology classification as a proxy for the relative contribution of bright and faint pixels to the total galaxy flux. Here we follow the prescriptions given by Lotz et al. (2004) to compute G. We first order the sky-subtracted pixels from the lowest absolute pixel intensity to the highest one. The Gini coefficient can be then computed as:

$$G = \frac{1}{\overline{|f|}n(n-1)} \sum_{i=1}^{n} (2i - n - 1)\,|f_i| \tag{14}$$

where n is the number of pixels, $\overline{|f|}$ is the average absolute pixel intensity and f_i is the value of the pixel i once the pixels have been ranked by their absolute brightness. The possible values of G range from 0 to 1. A galaxy where the total flux is equally distributed among all pixels would have $G = 0$, and $G = 1$ would be found if one pixel was responsible of the total galaxy flux. Generally speaking, high values of G mean that most of the galaxy flux is localized in a few pixels, whereas low values are indicative of a more even distribution.

Although sophisticated methods like segmentation maps can be used to define pixels belonging to the galaxy (Lotz et al. 2004), here we simply measure G within the R25 elliptical apertures from the RC3 or NED in all bands. While a precise centering is a delicate point when computing the asymmetry, as explained in Section 3.3.2, the Gini coefficient is not affected by this issue. However, this is a double-edged sword, since G only tells us about the relative contribution of pixels with different intensities to the total flux, regardless of their spatial distribution within the galaxy. In other words: objects with entirely different morphologies may yield very similar values of G (see e.g. Fig. 2 in Abraham et al. 2003). While the usefulness of G as a standalone morphological parameter might be somewhat limited depending on the rest-frame wavelength of observation, its real power emerges when comparing it with other estimators, as we will see later.

As with the asymmetry, we have analyzed the impact on G of using the Petrosian radius instead of the R25 one. As explained in Lotz et al. (2004), including too many sky pixels in the aperture will tend to increase G, while leaving out emission from the outer parts of the galaxy will systematically decrease it. We have found that, on average, $\langle G_{R25} - G_{r_P} \rangle = 0.11$, with a typical scatter of ± 0.10. Since $G \sim 0.6$ for our galaxies (see Fig. 8), such an offset represents a relative difference of $\sim 18\%$. By visually inspecting the images with the R25 and Petrosian ellipses over-plotted, we have verified that the Petrosian radius usually leaves out significant emission from the outer regions of galaxies. The amount of missed light depends strongly on the radial light profile, and indeed increases monotonically with light

concentration and/or the Sérsic index (Graham et al. 2005). While r_P usually encloses almost all the emission in late-type spirals, prominent bulges and bright inner arms in earlier ones tend to decrease r_P, and with it G as well. Performing the measurements within n times the Petrosian radius would not help, as it would probably introduce too many sky pixels in late-type spirals where r_P alone is already a sufficiently large aperture.

Perhaps the most flagrant case in our sample is NGC 4736, a Sab spiral with a small bright inner ring that dominates the overall emission at all wavelengths. The Petrosian radius at $\eta = 0.2$ is $60''$, which is precisely the radius of the inner ring. Having a Gini coefficient of ~ 0.5 within r_P, this galaxy would hardly qualify as being particularly concentrated. However, the emission actually extends much further out, with clearly visible structures lying $350''$ away from the center at all wavelengths. The R25 ellipse comfortably includes all this emission, and yields $G > 0.8$, which reflects more faithfully the true nature of this object.

Since the dependence of r_P on light concentration may bias the resulting values of G as a function of Hubble type, and in order to properly handle objects like NGC 4736, we have opted to keep the R25 ellipses as our measurement apertures.

The derived values of the Gini coefficient can be seen in Table 8. We have flagged values of G as unreliable when the FWHM at a given band is larger than $0.5\,\mathrm{kpc}$ at the particular distance of each galaxy, as we did for the asymmetry. The Gini coefficient is expected to decrease at very low signal-to-noise ratios, so the values of G measured on the 2MASS images should be taken with care, as they could be underestimated.

3.3.4. The second-order moment of light.

The total second-order moment of the light in a galaxy is defined as:

$$M_{\mathrm{tot}} = \sum_{i=1}^{n} M_i = \sum_{i=1}^{n} f_i \left[(x_i - x_c)^2 + (y_i - y_c)^2 \right] \tag{15}$$

where f_i is the flux of the pixel located at (x_i, y_i), and (x_c, y_c) are the coordinates of the galaxy's center. Lotz et al. (2004) suggest using the normalized second-order moment of the pixels responsible of the brightest 20% of the total galaxy flux:

$$\overline{M}_{20} = \log \left(M_{20}/M_{\mathrm{tot}} \right) \tag{16}$$

where M_{20} is computed by ranking the pixels in order of decreasing intensity, and then summing M_i over the brightest pixels until $\sum f_i = 0.2 f_{tot}$.

The values of $\overline{M}_{20}$ are always negative. Centralized emission yields lower (i.e. more negative) values than more extended emission. The advantage of $\overline{M}_{20}$ over the concentration index C_{42} is that since $\overline{M}_{20}$ depends on the squared distance to the galaxy's center, it is more sensitive to the spatial distribution of bright regions than C_{42}, which is usually heavily influenced by the bulge. We measured $\overline{M}_{20}$ within the RC3 elliptical apertures, whose centers were iteratively shifted in order to minimize M_{tot}, as suggested by Lotz et al. (2004). These authors also found that $\overline{M}_{20}$ can be unreliable at poor spatial resolutions, so we again impose the same same limit of $0.5\,\text{kpc}$ for the physical resolution.

When comparing the values of $\overline{M}_{20}$ measured inside the optical ellipses with those obtained within the Petrosian ellipses, we find that $\langle \overline{M}_{20,R25} - \overline{M}_{20,r_P} \rangle = -0.15$, with an rms of ± 0.22. Considering that the second-order moment typically ranges between -1 and -4 for the SINGS galaxies (see Fig. 8), this offset translates into a relative difference of just a few percent. The fact that $\overline{M}_{20}$ is slightly smaller when measured inside the optical ellipses is expected, since the outer regions of galaxies between r_P and $R25$ will contribute to increase M_{tot} but not necessarily M_{20}, thus decreasing the normalized moment $\overline{M}_{20}$.

4. Results

4.1. Asymptotic magnitudes

The asymptotic magnitudes are plotted in Fig. 4 as a function of wavelength, with galaxies grouped according to their morphological type. The results presented here are fully consistent with those obtained by Dale et al. (2007) using aperture photometry. Indeed our asymptotic magnitudes are in excellent agreement with the aperture magnitudes of Dale et al. (2007). We find that the average difference $\left| \text{mag}_{\text{asymp}} - \text{mag}_{\text{aper}} \right|$ at each band is typically below $\sim 0.07\,\text{mags}$, with a dispersion of $\sim 0.2\,\text{mags}$.

The $4000\,\text{Å}$ break is evident in all panels, and its amplitude decreases towards late morphological types. The ratio of the total infrared to UV luminosity also varies with morphological type, reaching a maximum value in Sb-Sbc spirals (Dale et al. 2007), which can be interpreted in terms of varying attenuation (Gordon et al. 2000; Witt & Gordon 2000; Buat et al. 2005). This change of the TIR-to-UV ratio is accompanied by a variation in the slope of the UV spectra, in the sense that spirals with lower TIR-to-UV ratios also have flatter UV spectra. This means that the (FUV−NUV) color can be used as an indirect tracer of the attenuation, not only in starburst galaxies (Calzetti et al. 1994), but also in normal star-forming galaxies, although with larger dispersion (Boissier et al. 2007; Gil de Paz et al. 2007; Paper II). Note, however, that part of the UV reddening seen in early-type

disks is not entirely due to the effect of dust, but also to their intrinsically redder old stellar populations (Cortese et al. 2008). Interestingly, most of the variations in the SEDs for S0/a galaxies and later are mostly driven by changes in the observed UV emission, rather than the FIR one (Dale et al. 2007). The ratio of $F_{160\mu m}/F_{3.6\mu m}$ varies by a factor of 20, roughly between 10 and 200, whereas $F_{FUV}/F_{3.6\mu m}$ spans three orders of magnitude, between 0.001 and 1.

It is also worth noting that while the SEDs of elliptical and lenticular galaxies look very similar in the optical and near-IR range, they differ significantly in the mid- and far-IR, in the sense that S0 galaxies tend to be more luminous in the infrared. Indeed, the two ellipticals showing the largest infrared fluxes in Fig. 4 seem to be rather peculiar. NGC 0855 shows structured emission in the mid-IR, and NGC 3265 exhibits a slightly disturbed optical morphology, and also optical emission lines indicating some level of star formation (Dellenbusch et al. 2007).

Another evident feature in these SEDs is the $8\,\mu m$ emission due to PAHs. It is most pronounced in Sb-Sd spirals, and seems to be almost absent in Sdm and irregulars and, to a lesser extent, in S0/a-Sab ones. These variations can be understood in terms of differences in the abundance of PAHs (see e.g. Engelbracht et al. 2005, 2008 and references therein), although a detailed modeling of the emitting properties of dust is required to properly translate these flux ratios into chemical abundances (Draine et al. 2007).

It is instructive to examine the relative contribution of the bulge (or pseudo-bulge) and the disk to the global SEDs of these galaxies (Fig. 5). By inspecting the FUV and $3.6\,\mu m$ profiles, we visually determined for each galaxy the radius separating the regions dominated by the bulge and disk emission. At this radius a sharp change in the (FUV$-3.6\,\mu m$) color is usually seen, due to the steeper rise of the $3.6\,\mu m$ luminosity above the main exponential disk, as well as to the central decrease in the FUV luminosity (see Section 4.2). Of course, the transition from the bulge and disk is actually gradual, so the SEDs presented here should be just understood as bulge- or disk-dominated. Note, however, that the mid- and far-IR within the bulge likely arises from the disk, although circumstellar dust in the bulge itself may also contribute.

The largest variations appear in the optical and UV bands. On average, $F_{FUV}/F_{3.6\mu m}$ in bulges appears to be one order of magnitude fainter than in the galaxies as a whole. Of course, the opposite behavior is seen in the disks. The mid- and far-infrared emission, relative to the $3.6\,\mu m$ one, also seems to lie systematically below the median global SEDs in the central regions than in the outer ones. In other words, both the UV emission associated with recent star formation and the infrared light arising from dust are more radially extended than the $3.6\,\mu m$ luminosity, which probes the underlying old stellar population. This will be

more clearly seen in the Section 4.3.1, where we will analyze the variation of the concentration index from the FUV to the FIR.

4.2. Radial profiles

The radial profiles of the SINGS galaxies show a wide range of morphologies, with multiple components such as bulges and pseudo-bulges, exponential disks, inner and outer disk truncations, antitruncations, etc. These features do not only vary among galaxies but also with wavelength for the same object. All the multi-wavelength radial profiles for the SINGS galaxies are shown in Fig. 6. Only the ones for NGC 3031 (M 81) are included in the printed version of the journal (see the on-line edition for the whole figure set), but they provide an overall glimpse of the different structures that are usually discerned in the profiles of most spiral galaxies.

The profiles of NGC 3031 in the far- and near-UV show a sharp inner cutoff at $\sim 200''$, which imposes an upper limit of $\sim 1\,\mathrm{Gyr}$ for the last epoch of substantial star formation in the central part of the disk, since that is the typical lifetime of stars dominating the UV emission. These inner-truncated disks appear to be rather common in early-type spirals and could result from gas exhaustion in the central regions of these galaxies. These features warn against using a simple exponential profile when performing bulge-disk decompositions, as the disk might not extend to the very center of these galaxies (at least not in a disk populated by stars younger than a few Gyr). Indeed, based on optical surface brightness profiles, Kormendy (1977) already proposed the use of such inner-truncated exponential functions, and Baggett et al. (1998) applied that idea to a larger sample of galaxies. The (FUV−NUV) color exhibits an interesting behavior in the bulge. It initially becomes redder as we get closer to the center, from $(\mathrm{FUV} - \mathrm{NUV}) = 0.6$ at $r = 200''$ to 1.8 at $r = 50''$. However, for $r < 50''$ the UV color gets progressively bluer again, reaching $(\mathrm{FUV} - \mathrm{NUV}) = 1$ at the center. This could be due to the so-called UV-upturn, that is, the flux increase from $\lambda \simeq 2000\text{Å}$ to $\lambda \simeq 1200\text{Å}$ seen in the UV spectra of old stellar populations (see e.g. O'Connell 1999 and references therein). Indeed, E/S0 galaxies usually get increasingly bluer in the UV towards the center (Ohl et al. 1998). This bluer UV emission is thought to arise from low-mass, helium-burning stars at the end of the horizontal branch, since these stars usually have thin envelopes that leave their hot cores exposed. Note that M 81 harbors an active galactic nucleus (Peimbert & Torres-Peimbert 1981), whose influence in the UV color cannot be discarded, although its effects −if present− would be probably limited to the very center of the galaxy (Marcum et al. 2001).

In the optical and near-infrared, the bulge profile smoothly merges with the inner expo-

nential disk, which is followed by a secondary, downward-bending exponential beyond $\sim 500''$ in the case of NGC 3031. This is the most common type of truncation in spiral disks (Pohlen & Trujillo 2006). The truncation is sharpest in the UV, and becomes progressively smeared out in the optical and near-IR. Inside the truncation radius, the disk scale-length is larger in the UV than in the near-IR, thus leading to a blueing with increasing radius, as is expected from an inside-out growth scenario of disk formation (see e.g. de Jong 1996; Boissier & Prantzos 2000; Muñoz-Mateos et al. 2007). However, beyond the truncation radius the trend reverses, with the stellar populations getting redder as the galactocentric distance increases. This change in the color gradient has been indeed found to be a common feature in truncated disks (Bakos et al. 2008). The behavior seen in Fig. 6 is in agreement with the predictions of the models of Rŏskar et al. (2008), who argue that the outer exponential could be populated by old stars formed closer to the center of the galaxy, and later scattered outwards by spiral arms.

While the change of slope in the profiles of NGC 3031 is subtle at the $3.6\,\mu$m and $4.5\,\mu$m bands, it becomes more pronounced at $5.8\,\mu$m and $8.0\,\mu$m, which probe the emission arising from PAHs. The break gets even sharper at the $24\,\mu$m band, dominated by hot dust emission, and then becomes less pronounced at $70\,\mu$m and $160\,\mu$m, although the blurring effect due to the increasingly large PSF must be also taken into account. When comparing the FIR profiles measured on the IRAC and MIPS images after matching their PSFs with that of the $160\,\mu$m band, we verified that the break was still sharpest at $24\,\mu$m, meaning that the observed variations in the break sharpness cannot be entirely due to resolution effects. Note that in terms of the observed flux, the infrared profiles shown here do not only depend on the radial distribution of dust itself, but also on that of the heating sources (see Paper II).

Finally, there is one last feature in the profiles of NGC 3031 that only shows up in the FUV and NUV bands: an extended, shallower component beyond $\sim 800''$. The GALEX images reveal structured UV emission in the outermost regions, and this galaxy has been indeed classified as an extended UV disk (Thilker et al. 2007), a phenomenon first discovered in M 83 (Thilker et al. 2005) and NGC 4625 (Gil de Paz et al. 2005). These extended components are most easily detected in the UV partly because of the higher surface brightness sensitivity at those wavelengths. Underlying stellar emission may be seen at other wavelengths, although the UV-nIR colors tend to be blue (Thilker et al. 2007). The XUV emission in NGC 3031 seems to be tidally structured, as a result of the interaction with other galaxies belonging to the M 81 group. However, in many other XUV-disks the organized filamentary UV emission does seem to arise from the outward propagation of spiral waves, instead of tidal interactions. In this sense, Bush et al. (2008) argue that such a phenomenon can take place in spirals with pre-existing extended HI disks without the need of invoking the presence of a companion.

4.3. Morphology

Quantifying galaxy morphology at different wavelengths is not only useful to better understand the spatial distribution of the different components of galaxies, but also to automate morphological classification in modern surveys (see e.g. Scarlata et al. 2007). Most of the work that has been done in this field has been carried out in the optical range, although some authors have also considered the UV range (Kuchinski et al. 2000, 2001; Burgarella et al. 2001; Lauger et al. 2005; Taylor-Mager et al. 2007). These authors found that galaxies generally exhibit larger asymmetries and lower concentration indices in the UV than in the optical, since the UV traces recent star formation, which has a clumpier and more radially extended spatial distribution than the intermediate-age stars seen in the optical. These considerations are particularly important for comparisons with samples of galaxies at $z \sim 1-2$, as optical observations of these objects probe the restframe UV.

With the advent of *Spitzer*, similar analysis are now possible in the IR as well. Bendo et al. (2007) computed non-parametric estimators on the $3.6\,\mu$m and $24\,\mu$m images of the SINGS galaxies, finding that the $24\,\mu$m emission arising from very hot dust is usually more extended and asymmetric in late-type galaxies than in early-type ones, even when the $3.6\,\mu$m data are degraded to the same resolution as the $24\,\mu$m data.

In this section we provide non-parametric morphological estimators for the SINGS galaxies from the FUV to the FIR. While an exhaustive analysis of the morphological implications of these results is beyond the scope of this paper, a brief discussion is also presented.

4.3.1. Morphology as a function of wavelength

Concentration index. In Fig. 7 we show how C_{42} varies with wavelength for galaxies of different morphological types. Dashed lines are used when r_{20} is smaller than the innermost point of our profiles ($6''$ at $24\,\mu$m and $12''$ at $70\,\mu$m and $160\,\mu$m). In order to detect possible biases due to the spatial resolution, we show red (blue) lines with the median values for the galaxies further (closer) than the median distance of the galaxies within each morphological bin. These median distances were individually computed for each bin of Hubble types, since late-type galaxies in the sample are closer on average than early-type ones. The values are $17\,$Mpc (E-S0), $17\,$Mpc (S0/a-Sab), $15\,$Mpc (Sb-Sbc), $9\,$Mpc (Sc-Sd) and $4\,$Mpc (Sdm-Irr).

Ellipticals and lenticulars exhibit $C_{42} \gtrsim 3$ at all wavelengths, but spirals present a much more varied behavior. Their concentration indices typically lie below 3 in the UV, due to the contribution of young stars spread across the disk. Then it suddenly rises in the optical, as the bulge dominates the overall light concentration longward of the Balmer break

($\lambda \sim 0.36\mu$m). Early-type spirals usually show central depletions in their UV emission, with inner-truncated disks, while in the optical and near-IR the bulge is more prominent, hence the large discontinuity between C_{42}(UV) and C_{42}(opt). Such a jump can be enhanced by the presence of rings (Lauger et al. 2005). The difference becomes progressively less pronounced in later Hubble types, as the transition from the central bulge (or pseudo-bulge) and the disk becomes more gradual.

The concentration index rises slowly from the optical to the near-IR, and then drops again at $5.8\,\mu$m and $8.0\,\mu$m, since these bands probe the spatial distribution of PAHs. The amplitude of this 'break' in C_{42} decreases in late-type spirals, but is still sharper than the one between the UV and the optical bands. While Sc spirals and later usually exhibit low values of C_{42}, typically below ~ 3, there is much more dispersion in galaxies or earlier types towards larger concentration indices. By analyzing the $24\,\mu$m morphologies of the SINGS galaxies, Bendo et al. (2007) suggested that bars might increase light concentration at $24\,\mu$m by enhancing nuclear star formation activity, although the statistical evidence was not compelling.

There are some galaxies in each panel having significantly larger infrared concentration indices than the remaining galaxies of the same morphological type. This is the case of NGC 1291 (S0/a), NGC 1512 (Sa), NGC 1097 (Sb), NGC 3351 (Sb) and NGC 4536 (Sbc). These galaxies exhibit signs of very intense nuclear and/or circumnuclear emission when inspected at $8\,\mu$m and $24\,\mu$m, hence their unusually large concentrations. Note that although NGC 1291 has an outer ring, the nuclear emission dominates the total luminosity at $24\,\mu$m and $70\,\mu$m, hence the large values of C_{42} at these bands.

The galaxy exhibiting high values of C_{42} in the panel for Sc-Sd spirals is NGC 5033. Unlike the galaxies mentioned above, which depart from the general trends only in the infrared, NGC 5033 is above all Sc-Sd galaxies already in the optical. A visual inspection shows no sign of any intense nuclear emission, but reveals however a rather prominent bulge for an Sc spiral. The multiband radial profiles show indeed that the light distribution of this galaxy has a non-negligible contribution from the central bulge, which is absent in other galaxies of the same morphological bin. The fact that this is a Seyfert galaxy might contribute to its high concentration in the infrared.

The results presented here agree with those presented in other papers in the literature. As an example, Taylor-Mager et al. (2007) performed a quantitative analysis of the rest-frame UV and optical morphology of 199 nearby galaxies, using imagery from GALEX, HST and ground-based telescopes. They found that ellipticals and lenticulars typically have $C_{42} \simeq 4$, they same average value obtained here. Although these authors noted a drop-off in C_{42} shortward of the Balmer break in E-S0 galaxies −a feature that is absent here−, they

warned against over-interpreting this feature, given the low S/N of those red galaxies in the UV. They do find a clear trend with wavelength in Sa-Sc spirals, with C_{42} rising from ~ 2 in the FUV to ~ 3 in the I band. The trend we observe is fully consistent with theirs, although our finer bins in morphological types reveal that the wavelength dependence of C_{42} actually varies within Sa-Sc galaxies, being less pronounced in later types. Our typical concentration indices for irregulars agree well with those of Taylor-Mager et al. (2007) (roughly 2.5). While these authors study in great detail the morphology of mergers, such an analysis is not possible here, since there are not major mergers in our sample and the few galaxies with low mass companions have those objects deliberately masked out.

Asymmetry. In Fig. 7 we also show the dependence of the asymmetry on wavelength. Dashed lines indicate that the FWHM at a given wavelength corresponds to a physical size larger than $0.5\,$kpc at the distance of each galaxy. As expected, ellipticals and lenticulars exhibit low asymmetries at all wavelengths, typically below 0.15. In S0/a galaxies and later there is a clear trend with wavelength: A reaches a maximum in the FUV, where the emission is dominated by recent star formation. As we move towards longer wavelengths in the optical and near-IR, the intermediate-age and old stars from the bulge and halo −which are more smoothly distributed across the disk than young ones − progressively decrease the global asymmetry of the galaxies. PAHs make their appearance at $5.8\,\mu$m and $8.0\,\mu$m, increasing the asymmetry again. Hot dust associated with clumps of star formation tend to increase A even more at $24\,\mu$m. This U-like shape of the A_λ distribution is enhanced as we progress along the Hubble sequence: intermediate- and late-type spirals become progressively more asymmetric in the UV-optical range, as well as in the mid-IR. Note that the increase in asymmetry in the UV and mid-IR bands is the opposite of what would be expected from the degradation of the PSF, thus reassuring that these changes in A are real. However, the drop-off seen at $70\,\mu$m and $160\,\mu$m for some galaxies is most likely the result of the poorer resolution.

The outlier in the panel for Sc-Sd galaxies is NGC 5474. This companion of M 101 (Drozdovsky & Karachentsev 2000) shows a strongly disturbed morphology, with a large plateau shifted southward with respect to the bright central disk, hence its large asymmetry. Interestingly, NGC 5474 looks like a normal spiral when viewed in the UV, thus not showing much departure from the typical asymmetries in that spectral range.

Our multi-wavelength asymmetries seem to be consistent with other published values for nearby galaxies. We take again as an example the work of Taylor-Mager et al. (2007). As expected, they also conclude that E-S0 galaxies exhibit the lowest asymmetries. In Sa-Sc spirals, their asymmetries decrease from ~ 0.8 in the FUV to ~ 0.2 in the I-band. Once

divided by 2 −these authors do not include the 1/2 factor when computing the asymmetry−, these values nicely match the ones we have derived. The agreement is not as good in very late-type spirals and irregulars, our UV asymmetries being a bit larger in the UV, although with considerable dispersion.

Most galaxies show a small bump in the asymmetry at $3.6\,\mu$m and $4.5\,\mu$m. This feature becomes more evident in the latest Hubble types, and is most likely due to the large number of background sources detected in these bands. While our masking procedure eliminates sources that could potentially contaminate our profiles and magnitudes (see Section 3.1 and Fig. 2), these ubiquitous faint sources may still have a substantial impact on the asymmetry. This effect is expected to become more noticeable in galaxies with lower average surface brightness within the aperture used to compute the asymmetry (usually late-type ones). We do observe indeed a marked correlation between $A_{3.6,\ 4.5\mu\mathrm{m}}$ and the average surface brightness at those bands, a correlation that is not seen at other wavelengths (not shown).

Gini coefficient   In Fig. 8 we show how the Gini coefficient (and also $\overline{M}_{20}$) varies with wavelength and morphological type. As with the asymmetry, dashed lines are used when the FWHM does not allow resolving structures smaller than $0.5\,$kpc at the distance of each galaxy. In general, G tends to decrease from early- to late-type galaxies, especially in the optical and near-IR bands. However, the scatter is large, and the overlap between the values of G between adjacent bins of T type is considerable. No clear trend with wavelength can be inferred for galaxies earlier than Sab, but Sb spirals and later G apparently exhibits a mild wavelength dependence, in the sense that it seems to be larger in the UV and mid-IR (especially at $24\,\mu$m) than in the optical and near-IR[10]. What is the reason behind this modest trend with wavelength, despite the evident change in morphology among the bands considered here? In the optical and near-IR, pixels in the bulge contribute to a relatively large fraction of the total galaxy luminosity, the Gini coefficient being largest in early-type galaxies than in late-type ones. The morphology in the UV and the mid-IR is considerably different, yet the total galaxy luminosity can be still dominated by emission arising from a few pixels, but this time localized mainly in star-forming regions. As a result, G can reach values similar to or even larger than those in the optical and near-IR. Therefore, G is only expected to be correlated with central light concentration in the optical and near-IR (see Section 4.3.2).

Our Gini coefficients seem to be consistent with those in the literature. At $3.6\,\mu$m and $24\,\mu$m, the agreement between our values and those derived in Bendo et al. (2007) is excellent[11]. The average offset $\langle G_{Bendo} - G_{ours}\rangle$ is jsut -0.03 at $3.6\,\mu$m and 0.008 at $24\,\mu$m, the scatter being ~ 0.03 in both cases. In the optical, for the galaxies we have in common

with Lotz et al. (2004) our values of G are, on average, $\sim 15\%$ larger. This is most likely attributable to differences in the sizes of the regions used to perform the measurements. Lotz et al. compute G within segmentation maps whose extent depends on the Petrosian radius at $\eta = 0.2$, while we do it within the R25 ellipses, including emission that is missed by the Petrosian aperture. As discussed in Section 3.3.3, this can easily lead to systematic differences of 15-20% in the resulting values of G.

Second-order moment. Not surprisingly, the behavior of $\overline{M}_{20}$ is remarkably similar to that of C_{42} (see Fig. 7). Ellipticals and lenticulars exhibit $\overline{M}_{20} \sim -2.5$ across the whole wavelength range, which is indicative of highly-concentrated light distributions. On the contrary, most Sdm galaxies and irregulars tend to have $\overline{M}_{20} \gtrsim -1$. In spirals, $\overline{M}_{20}$ remains high in the UV, where most of the emission emerges from star-forming regions distributed across the disk. Longward of the Balmer break, $\overline{M}_{20}$ decreases abruptly, the decrement being more pronounced in early-type spirals than in late-type ones due to the larger bulge-to-disk ratios of the former. A second break happens in the mid-IR, where $\overline{M}_{20}$ increases again due to the emission of PAHs at 5.8 and $8.0\,\mu$m, and hot dust at $24\,\mu$m.

Our values of $\overline{M}_{20}$ agree well with published ones, both in the optical for the galaxies in common with Lotz et al. (2004), and at $3.6\,\mu$m and $24\,\mu$m in the study by Bendo et al. (2007).

4.3.2. Trends between the different morphological estimators

It is apparent from Figs. 7 and 8 that the most dramatic changes in C_{42} and $\overline{M}_{20}$ with Hubble type take place at the optical and near-IR. An obvious correlation shows up when plotting these morphological estimators at $3.6\,\mu$m against the morphological type (Figs. 9a and c). In Fig. 9b we plot the concentration index as a function of the absolute magnitude in that band, which is a proxy for the stellar mass of the galaxies. While both parameters are correlated for galaxies fainter than -21 mags, the trend breaks down at larger luminosities, since galaxies with $M_{3.6\mu m} \sim -22$ are ellipticals, lenticulars and early-type spirals, the former being typically more concentrated than spirals with similar stellar masses. A very similar result was obtained by Boselli et al. (1997) for Virgo galaxies. These authors found

---

[10]Note that the values of G in the 2MASS bands could be underestimated, due to the poorer S/N ratio of those images compared to the rest of the data.

[11]Note that Bendo et al. matched the PSF and the plate-scale of the $3.6\,\mu$m images to those of the $24\,\mu$m ones.

a somewhat tighter trend between C_{42} and the K-band magnitude at the low luminosity regime, since their sample better probed that luminosity range. While the SINGS galaxies are quite homogeneously distributed in terms of morphological types, the distribution in near-IR luminosity is more peaked around relatively bright objects. The trend between $\overline{M}_{20}$ and the absolute magnitude does not exhibit the upward bending seen in panel (b) with the concentration index, since both parameters are not linearly correlated, as we shall see below.

In Fig. 10 we can see that at $3.6\,\mu$m, and also in the optical bands, C_{42} and $\overline{M}_{20}$ are very tightly correlated, the slope of the trend increasing from late- to early-type spirals. We have used the boundary-fitting code of Cardiel (2009) to fit third-order polynomials to the upper and lower envelopes of the data-point distribution at $3.6\,\mu$m. These curves are replicated in all panels for the ease of comparison. The trend presents an elbow located at $\overline{M}_{20} \sim -2, C_{42} \sim 3$, in good agreement with other works in the literature (Lotz et al. 2004; Scarlata et al. 2007). The different slopes at both sides of the elbow can be attributed to the varying contribution of the bulge and disk to the overall light distribution (Scarlata et al. 2007). Indeed, most points leftwards of the elbow correspond to Sc spirals and later, whereas those at larger concentration values correspond to Sbc spirals and earlier. Since this trend is shaped by the varying B/D ratio, it also holds in the optical bands, which still trace the underlying stellar population, but it breaks down in the UV and the mid-IR, which trace recent star formation. Both indicators show that at these wavelengths galaxies exhibit much more extended light distributions.

In Fig. 11 we compare the Gini coefficient and $\overline{M}_{20}$. We have fitted two straight lines to the boundaries of the data-point distribution at $3.6\,\mu$m. A clear correlation is seen in the optical and near-IR, in agreement with previous studies (Abraham et al. 2003; Lotz et al. 2004). The interpretation of G as a proxy for light concentration is valid in these bands simply because bright pixels are mainly located in the bulge. Therefore, to first order the relative contribution of bright pixels to the total luminosity closely depends on the bulge-to-disk ratio, which in turn is correlated with central light concentration. But this is no longer valid as soon as we peer into the UV and mid-IR regimes, where galaxies usually have larger values of G and $\overline{M}_{20}$. This time, most bright pixels are associated with star-forming regions, so G is not correlated with central concentration any more.

Interestingly, when viewed at $24\,\mu$m normal galaxies occupy the same region in the G-$\overline{M}_{20}$ plane as the ultra-luminous infrared galaxies (ULIRGs) of Lotz et al. (2004) in the R band. This was already noted by Bendo et al. (2007), and we confirm that this also occurs in the FUV and $8\,\mu$m, although to a lesser extent. The same behavior is seen in the G-A plane (not shown), where normal galaxies exhibit high asymmetries and Gini coefficients at $24\,\mu$m, similar to those of ULIRGs in the optical. However, this should not be blindly generalized.

For instance, the R-band data for ULIRGS in Lotz et al. (2004) fill the upper-left region of the C_{42}-$\overline{M}_{20}$ plane, but our normal galaxies occupy a different area of the plot when observed at $24\,\mu$m (Fig. 10).

The relation between the concentration index and the asymmetry is presented in Fig. 12. The dynamic range in C_{42} and A is largest in the FUV, where different morphological types clearly delineate a sequence in the C_{42}-A plane, although with a certain overlap. In the optical and near-IR bands not only the dynamic range is smaller, but also the relative arrangement of data-points differs. For instance, Sb-Sbc spirals appear to be of later Hubble types when viewed in the FUV, but merge with S0/a-Sab galaxies at longer wavelengths. Note that, as stated above, the systematic upward shift in the asymmetries of Sdm-Irr galaxies at $3.6\,\mu$m is likely due to background sources. In the mid-IR the C_{42}-A sequence lengthens again, the main difference with respect to the FUV being the presence of sources with high central concentrations, due to intense (circum)nuclear emission.

Unlike in the previous diagrams, where galaxies shift to an entirely different locus in the parameter space when observed in the UV or mid-IR, in the C_{42}-A plane they apparently move along roughly the same diagonal sequence. At $24\,\mu$m there are a few points with slightly larger asymmetries at fixed C_{42} in comparison with the optical bands, but in general the displacement takes place diagonally. In Fig. 13 we have plotted all data-points for different bands simultaneously. Besides the six bands shown in Fig. 12, we have added the NUV as well for a better wavelength sampling. The bulk of the data-points lie within the boundaries delineated by the dashed lines, regardless of the wavelength. Many ULIRGs would probably lie in the upper-right region of the plot.

5. Conclusions

We have obtained surface brightness profiles for the SINGS galaxies all the way from the FUV to the FIR, in order to map the radial structure of stars and the interstellar medium. The profiles were measured on UV images from GALEX, optical data from KPNO, CTIO and SDSS, near-IR images from 2MASS, and mid- and far-IR data from the IRAC and MIPS instruments onboard *Spitzer*. The multi-wavelength data-set released here may be used in a variety of galactic structure studies beyond those presented in this paper, including morphological classification, bulge-disk decomposition, analysis of disk truncations or comparison with the output of disk-formation models, among others.

From the growth curves we have computed asymptotic magnitudes at different wavelengths. The resulting SEDs lead to similar results as those found by Dale et al. (2007)

using aperture photometry. The 4000 Å break is seen to decrease from early- to-late type galaxies, reflecting changes in the mean age of the underlying stellar populations. The total infrared-to-UV ratio, which can be used as a proxy for the UV attenuation, also varies with morphological type, being maximum in Sb-Sbc spirals. The $8\,\mu$m feature associated with PAHs stands out in Sb-Sd galaxies, and is less prominent in earlier and later types, especially in Sdm and Im galaxies.

We have also analyzed the wavelength dependence of four non-parametric morphological estimators: the concentration index, the asymmetry, the Gini coefficient and the normalized second-order of the brightest 20% of the galaxy's flux. Ellipticals and S0s exhibit very small asymmetries, large concentration indices and small (i.e. very negative) values of $\overline{M}_{20}$ across the whole spectral range considered here. Disk-like galaxies, however, display larger variations, indicating the presence of several stellar and dust components with different spatial distributions. Localized star-forming complexes dominate the FUV emission, giving galaxies a clumpy appearance at this band, where the asymmetry is therefore maximum. Since star-formation is usually widespread across the whole disk, the concentration index exhibits a minimum value in the FUV. Older stellar populations are arranged in a more uniform disk and a central bulge, thus decreasing the asymmetry and increasing the concentration index in the optical and near-IR bands. This trend is reversed when PAHs show up at $5.8\,\mu$m and $8.0\,\mu$m, since galaxies again exhibit a patchier and more radially extended appearance. The same applies to the $24\,\mu$m band, dominated by hot-dust emission.

In the optical and near-IR, the Gini coefficient is correlated with light concentration. Galaxies with more centrally concentrated light distributions have most of their flux emerging from a few pixels, and exhibit therefore high values of G. However, this trend does not hold in the UV and mid-IR, where galaxies exhibit low concentration indices yet high Gini coefficients, since the few pixels dominating the total emission are now distributed all over the disk.

The data-set presented in this paper serves as the foundation for other ongoing and more detailed studies we are carrying out. In the accompanying paper (Muñoz-Mateos et al. 2009) we provide an in-depth analysis of the radial distribution of dust properties in the SINGS galaxies, ranging from attenuation to dust column density, as well as PAH abundance, dust-to-gas ratio and the properties of the heating sources. These profiles are also being used to constrain the predictions of the disk-evolution models of Boissier & Prantzos (2000). The results will be presented in a forthcoming paper, focusing on the radial variation of the star formation history and its connection with the inside-out assembly of disks.

Facilities: GALEX, Sloan, CTIO:1.5m, KPNO:2.1m, FLWO:2MASS, CTIO:2MASS, *Spitzer*

A.   Recalibrating the optical data

As mentioned in Section 2.2, a large subset of the original SINGS optical images suffer from zero-point offsets whose origin has not been fully identified. While some of the structural properties presented in this paper, such as concentration indexes or asymmetries, do not depend on these calibration issues, estimating these offsets is essential if one wishes to employ these data in stellar population studies.

The optical images were recalibrated using the catalog of aperture photometry of Prugniel & Heraudeau (1998). This compilation merges photometric data from the literature obtained through different methods: photoelectric photometry with diaphragms, simulated aperture photometry from radial profiles and aperture measurements on images.

Let $F_{\mathrm{ref},\lambda}(r)$, $F_{\mathrm{ours},\lambda}(r)$ and $F_{\mathrm{true},\lambda}(r)$ be the fluxes enclosed inside a circular aperture of radius r in the reference data, in our images and in the actual galaxy, respectively. We can write the following:

$$F_{\mathrm{true},\lambda}(r) \;\; = \;\; C_\lambda F_{\mathrm{ours},\lambda}(r) \tag{A1}$$

$$F_{\mathrm{true},\lambda}(r) \;\; = \;\; F_{\mathrm{ref},\lambda}(r) - B_\lambda r^2 \tag{A2}$$

$$\frac{F_{\mathrm{ref},\lambda}(r)}{r^2} \;\; = \;\; C_\lambda \frac{F_{\mathrm{ours},\lambda}(r)}{r^2} + B_\lambda \tag{A3}$$

In Eq. A1 we are assuming that since we have masked most relevant foreground and background objects, the shape of our radial profiles is essentially correct, so we only need to multiply our data by a certain recalibration factor C_λ in order to get the actual fluxes. As for the data from the literature, in Eq. A2 we suppose that they are not affected by zero-point biases, but we allow for possible errors in the background subtraction through the term $B_\lambda r^2$. While in our frames there are always enough sky areas free from emission from the galaxy, this might not be necessarily the case in some of the reference data from the literature. Also, differences in the amount of background and foreground objects that have been subtracted should also scale roughly proportional to the aperture area, provided that these sources are uniformly distributed throughout the field of view; to some extent the $B_\lambda r^2$ term can also account for this effect, if present. The sign of B_λ can be either positive or negative depending on whether the background in the reference data has been over- or under-subtracted. Should the assumptions above be correct, Eq. A3 implies that the recalibration factor C_λ can be obtained from a simple linear fit.

We made use of the VizieR service (Ochsenbein et al. 2000) to query the catalog of Prugniel & Heraudeau (1998) and retrieve all the available aperture photometry for our galaxies. All magnitudes were homogenized (in terms of filter systems) and converted to AB units using the color transformations and AB magnitudes of Vega provided in Fukugita et al. (1995). We then used the IRAF task PHOT to perform aperture photometry on our images, using the same sets of circular apertures as those compiled from the literature. The recalibration factors were then obtained by comparing both sets of data and applying a linear fit (Eq. A3).

The resulting values appear in Table 9. As an example, Fig. 14 shows the results for NGC 1097 in the I band. The small numbers next to each data-point show the radius of the corresponding aperture in arcseconds. The behavior is clearly linear, although very small apertures can sometimes depart from the general trend, since they are prone to suffer from centering errors and seeing effects. These points were excluded from the final fit, as well as those showing different fluxes for exactly the same aperture size. When there was only one available photometric measurement at a given band, we assumed that $B_\lambda = 0$ in Eq. A3 and computed the calibration factor C_λ simply as the ratio of the reference flux and ours.

The statistical uncertainty of the recalibration factors yielded by the fitting procedure is typically less than 5%. This is the error of the recalibrated data relative to the original values found in the literature, which of course carry their own uncertainties. The latter are difficult to constrain, as they are not quoted in the catalog of Prugniel & Heraudeau (1998). Nevertheless, we reckon that a final zero-point error of 10%-15% should be adopted when using the recalibrated optical data. In Fig. 4 galaxies with SDSS data and those with recalibrated optical data are plotted together; the small dispersion constitutes a sanity check for our recalibration procedure. Note that recalibration factors are not provided for some SINGS galaxies (mainly dwarfs) that do appear in the catalog of Prugniel & Heraudeau (1998), since the resulting optical data seemed to be largely discrepant from the overall SED.

REFERENCES

Abraham, R. G., Tanvir, N. R., Santiago, B. X., Ellis, R. S., Glazebrook, K., & van den Bergh, S. 1996a, MNRAS, 279, 47

Abraham, R. G., van den Bergh, S., Glazebrook, K., Ellis, R. S., Santiago, B. X., Surma, P., & Griffiths, R. E. 1996b, ApJS, 107, 1

Abraham, R. G.; van den Bergh, S., & Nair, P. 2003, ApJ, 588, 218

Adelman-McCarthy, J. K., et al. 2008, ApJS, 175, 297

Baggett, W. E., Baggett, S. M., & Anderson, K. S. J. 1998, AJ, 116, 1626

Bakos, J., Trujillo, I., & Pohlen, M. 2008, ApJ, 683, 103

Bendo, G. J., et al. 2006, ApJ, 645, 134

Bendo, G. J., et al. 2007, MNRAS, 380, 1313

Bershady, M. A., Jangren, A., & Conselice, C. J. 2000, AJ, 119, 2645

Bertin, E., & Arnouts, S. 1996, A&AS, 117, 393

Boissier, S., Boselli, A., Buat, V., Donas, J., & Milliard, B. 2004, A&A, 424, 465

Boissier, S., & Prantzos, N. 2000, MNRAS, 312, 398

Boissier, S., et al. 2005, ApJ, 619, 83

Boissier, S., et al. 2007, ApJS, 173, 524

Boselli, A., Tuffs, R. J., Gavazzi, G., Hippelein, H., & Pierini, D. 1997, A&AS, 121, 507

Buat, V., et al. 2005, ApJ, 619, 51

Burgarella, D., Buat, V., Donas, J., Milliard, B., & Chapelon, S. 2001, A&A, 369, 421

Bush, S. J., Cox, T. J., Hernquist, L., Thilker, D., & Younger, J. D. 2008, ApJ, 683, 13

Cairós, L. M., Caon, N., Vlchez, J. M., González-Pérez, J. N., & Muñoz-Tuñón, C. 2001, ApJS, 136, 393

Calzetti, D., Kinney, A. L., & Storchi-Bergmann, T. 1994, ApJ, 429, 582

Cardiel, N. 2009, MNRAS, 396, 680

Cohen, M., Wheaton, Wm. A., & Megeath, S. T. 2003, AJ, 126, 1090

Conselice, C. J., Bershady, M. A., & Jangren, A. 2000, ApJ 529, 886

Cortese, L., Boselli, A., Franzetti, P., Decarli, R., Gavazzi, G., Boissier, S., & Buat, V. 2008, MNRAS, 386, 1157

Cutri, R. M., et al. 2003, Explanatory Supplement to the 2MASS All Sky Data Release and Extended Mission Products, http://www.ipac.caltech.edu/2mass/releases/allsky/doc/explsup.html

Dale, D. A., et al. 2007, ApJ, 655, 863

de Jong, R.S. 1996, A&A, 313, 377

de Vaucouleurs, G. 1958, ApJ, 128, 465

de Vaucouleurs, G., 1977, Evolution of galaxies and stellar populations, ed. R. B. Larson, & B. M., Tynsley, Yale Univ. Obs., New Haven, 43

de Vaucouleurs, G., de Vaucouleurs, A., Corwin, H.G., Buta, R.J., Paturel, G., & Fouqué, P. 1991, Third Reference Catalogue of Bright Galaxies (RC3) (Springer-Verlag)

Dellenbusch, K. E., Gallagher, J. S., III, & Knezek, P. M. 2007, ApJ, 655, 29

Draine, B. T., & Li, A. 2007, ApJ, 657, 810

Draine, B. T., et al. 2007, ApJ, 663, 866

Drozdovsky, I. O., & Karachentsev, I. D. 2000, A&AS, 142, 425

Engelbracht, C. W., Gordon, K. D., Rieke, G. H., Werner, M. W., Dale, D. A., & Latter, W. B. 2005, ApJ, 628, 29

Engelbracht, C. W., Rieke, G. H., Gordon, K. D., Smith, J. D. T., Werner, M. W., Moustakas, J., Willmer, C. N. A., & Vanzi, L. 2008, ApJ, 678, 804

Engelbracht, C. W., et al. 2007, PASP, 119, 994

Erwin, P., Pohlen, M., & Beckman, J. E. 2008, AJ, 135, 20

Fall, S. M., & Efstathiou, G. 1980, MNRAS, 193, 189

Fazio, G. G., et al. 2004, ApJS, 154, 10

Ferguson, A. M. N., & Clarke, C. J. 2001, MNRAS, 325, 781

Freeman, K. C. 1970, ApJ, 160, 811

Fukugita, M., Shimasaku, K., & Ichikawa, T. 1995, PASP, 107, 945

Gil de Paz, A., & Madore, B. F. 2005, ApJS, 156, 345

Gil de Paz, A., et al. 2005, ApJ, 627, 29

Gil de Paz, A., et al. 2007, ApJS, 173, 185

Gini, C. 1912, reprinted in Memorie di Metodologia Statistica, ed. E. Pizetti & T. Salvemini (1955; Rome: Libreria Eredi Virgilio Veschi)

Gordon, K. D., Clayton, G. C., Witt, A. N., & Misselt, K. A. 2000, ApJ, 533, 236

Gordon, K. D., et al. 2007, PASP, 119, 1019

Governato, F., Willman, B., Mayer, L., Brooks, A., Stinson, G., Valenzuela, O., Wadsley, J., & Quinn, T. 2007, MNRAS, 374, 1479

Graham, A. W., Driver, S. P., Petrosian, V., Conselice, C. J., Bershady, M. A., Crawford, S. M., & Goto, T. 2005, AJ, 130, 1535

Heyer, M. H., Corbelli, E., Schneider, S. E., & Young, J. S. 2004, ApJ, 602, 723

Jarrett, T. H., Chester, T., Cutri, R., Schneider, S. E., & Huchra, J. P. 2003, AJ, 125, 525

Kennicutt, R. C., Jr., et al. 2003, PASP, 115, 928

Kent, S. M. 1985, ApJS, 59, 115

Kormendy, J. 1977, ApJ, 217, 406

Kuchinski, L. E., Madore, B. F., Freedman, W. L., & Trewhella, M. 2001, AJ, 122, 729

Kuchinski, L. E., et al. 2000, ApJS, 131, 441

Lauger, S., Burgarella, D., & Buat, V. 2005, A&A, 434, 77

Li, A., & Draine, B. T. 2001, ApJ, 554, 778

López-Sanjuan, C. et al. 2009, ApJ, 694, 643

Lotz, J. M., Primack, J., & Madau, P. 2004, AJ, 128, 163

MacArthur, L. A., Courteau, S., Bell, E., & Holtzman, J. A. 2004, ApJS, 152, 175

Marcum, P. M., et al. 2001, ApJS, 132, 129

Martin. D., et al. 2005, ApJ, 619 1

Muñoz-Mateos, J. C., et al. 2007, ApJ, 658, 1006

Muñoz-Mateos, J. C., et al. 2009, ApJ, 701, 1965 (Paper II)

Ochsenbein, F., Bauer, P., & Marcout, J. 2000, A&AS, 143, 23

O'Connell, R. W. 1999, ARA&A, 37, 603

Ohl, R.G., et al. 1998, ApJ, 505, 11

Oke, J. B. 1974, ApJS, 27, 21

Peimbert, M., & Torres-Peimbert, S. 1981, ApJ, 245, 845

Petrosian, V. 1976, ApJ, 209, 1

Pohlen, M., & Trujillo, I. 2006, A&A, 454, 759

Pohlen, M., et al. 2008, in ASP Conf. Ser. 396, Formation and Evolution of Galaxy Disks, ed. Funes, J. G., & Corsini, E. M. (San Francisco, CA: ASP), 183

Popescu, C. C., Misiriotis, A., Kylafis, N. D., Tuffs, R. J., & Fischera, J. 2000, A&A, 362, 138

Prugniel, Ph., & Heraudeau, Ph. 1998, A&AS, 128, 299

Reach, W. T., et al. 2005, PASP, 117, 978

Rieke, G. H., et al. 2004, ApJS, 154, 25

Robin, A. C., et al. 2007, ApJS, 172, 545

Rŏskar, R., Debattista, V. P., Stinson, G. S., Quinn, T. R., Kaufmann, T., & Wadsley, J. 2008, ApJ, 675, 65

Scarlata, S., et al. 2007, ApJS, 172, 406

Schade, D., Lilly, S. J., Crampton, D., Hammer, F., Le Fevre, O., & Tresse, L. 1995, ApJ, 451, 1

Schlegel, D. J., Finkbeiner, D. P., & Davis, M. 1998, ApJ, 500, 525

Sérsic, J. L., 1968, Atlas de Galaxias Australes (Córdoba, Argentina: Observatorio Astronómico)

Stansberry, J. A., et al. 2007, PASP, 119, 1038

Taylor-Mager, V. A., Conselice, C. J., Windhorst, R. A., & Jansen, R. A. 2007, ApJ, 659, 162

Thilker, D. A., et al. 2005, ApJ, 619, 79

Thilker, D. A., et al. 2007, ApJS, 173, 538

van der Kruit, P. C. 1979, A&AS, 38, 15

Walter, F., Brinks, E., de Blok, W. J. G., Bigiel, F., Kennicutt, R. C., Jr., Thornley, M. D., & Leroy, A. K. 2008, AJ, 136, 2563

Werner, M. W., et al. 2004, ApJS, 154, 1

Witt, A. N., & Gordon, K. D. 2000, ApJ, 528, 799

Wong, T., & Blitz, L. 2002, ApJ, 569, 157

Xilouris, E. M., Byun, Y. L., Kylafis, N. D., Paleologou, E. V., Papamastorakis, & J. 1999, A&A, 344, 868

York, D., et al. 2000, AJ, 120, 1579

Yoshii, Y., & Sommer-Larsen, J. 1989, MNRAS, 236, 779

Table 1.   Sample

Object name (1)	RA$_{2000}$ (h:m:s) (2)	DEC$_{2000}$ (d:m:s) (3)	2a (arcmin) (4)	2b (arcmin) (5)	P.A. (deg) (6)	E(B−V) (mag) (7)	dist (Mpc) (8)	T type (9)	Morphological type (10)	Optical data (11)	r_P (arcsec) (12)
NGC 0024	00 09 56.5	−24 57 47.3	5.8	1.3	46	0.020	8.2	5	SA(s)c	recal	152
NGC 0337	00 59 50.1	−07 34 40.7	2.9	1.8	310	0.112	25	7	SB(s)d	$\cdots$	63
NGC 0584	01 31 20.7	−06 52 05.0	4.2	2.3	55	0.042	28	−5	E4	recal	47
NGC 0628	01 36 41.8	15 47 00.5	10.5	9.5	25	0.070	11	5	SA(s)c	$\cdots$	239
NGC 0855	02 14 03.6	27 52 37.8	2.6	1.0	60	0.072	9.7	−5	E	$\cdots$	50
NGC 0925	02 27 16.9	33 34 45.0	10.5	5.9	282	0.076	9.3	7	SAB(s)d	recal	280
NGC 1097	02 46 19.1	−30 16 29.7	9.3	6.3	310	0.027	15	3	SB(s)b	recal	232
NGC 1266	03 16 00.7	−02 25 38.5	1.5	1.0	290	0.098	31	−2	(R')SB0(rs) pec	$\cdots$	34
NGC 1291	03 17 18.6	−41 06 29.1	9.8	8.1	345	0.013	9.7	0	(R)SB(s)0/a	recal	326
NGC 1316	03 22 41.7	−37 12 29.6	12.0	8.5	50	0.021	19	−2	SAB(s)0 pec	recal	197
NGC 1377	03 36 39.1	−20 54 08.0	1.8	0.9	92	0.028	24	−2	S0	recal	19
NGC 1404	03 38 51.9	−35 35 39.8	3.3	3.0	360	0.011	19	−5	E1	recal	36
NGC 1482	03 54 38.9	−20 30 08.8	2.5	1.4	283	0.040	25	−0.8	SA0$^+$ pec	recal	11
NGC 1512	04 03 54.3	−43 20 55.9	8.9	5.6	90	0.011	10	1	SB(r)a	recal	139
NGC 1566	04 20 00.4	−54 56 16.1	8.3	6.6	60	0.009	17	4	SAB(s)bc	recal	126
NGC 1705	04 54 13.5	−53 21 39.8	1.9	1.4	50	0.008	5.1	11	SA0- pec	recal	38
NGC 2403	07 36 51.4	65 36 09.2	21.9	12.3	307	0.040	3.2	6	SAB(s)cd	$\cdots$	351
Holmberg II	08 19 05.0	70 43 12.1	7.9	6.3	15	0.032	3.4	10	Im	$\cdots$	206
M81 Dwa	08 23 56.0	71 01 45.0	1.3	1.3	360	0.021	3.5	10	I?	$\cdots$	56 (B)
DDO 053	08 34 07.2	66 10 54.0	1.5	1.3	300	0.037	3.6	10	Im	$\cdots$	$\cdots$
NGC 2798	09 17 23.0	41 59 59.0	2.6	1.0	340	0.020	27	1	SB(s)a pec	recal	36
NGC 2841	09 22 02.6	50 58 35.5	8.1	3.5	327	0.016	14	3	SA(r)b	SDSS	175
NGC 2915	09 26 11.5	−76 37 34.8	1.9	1.0	309	0.275	3.8	90	I0	recal	71
Holmberg I	09 40 32.3	71 10 56.0	3.6	3.0	360	0.048	3.8	10	IAB(s)m	$\cdots$	162
NGC 2976	09 47 15.5	67 54 59.0	5.9	2.7	323	0.069	3.6	5	SAc pec	SDSS	140
NGC 3049	09 54 49.7	09 16 17.9	2.2	1.4	25	0.038	22	2	SB(rs)ab	SDSS	63
NGC 3031	09 55 33.2	69 03 55.1	26.9	14.1	337	0.080	3.6	2	SA(s)ab	SDSS	519
NGC 3034	09 55 52.2	69 40 46.9	11.2	4.3	65	0.159	3.9	90	I0	SDSS	50
Holmberg IX	09 57 32.0	69 02 45.0	2.5	2.0	40	0.079	3.6	10	Im	$\cdots$	109 (B)
M81 Dwb	10 05 30.6	70 21 52.0	0.9	0.6	320	0.080	5.3	10	Im	$\cdots$	54
NGC 3190	10 18 05.6	21 49 55.0	4.4	1.5	305	0.025	17	1	SA(s)a pec	SDSS	45
NGC 3184	10 18 17.0	41 25 28.0	7.4	6.9	135	0.017	8.6	6	SAB(rs)cd	SDSS	194
NGC 3198	10 19 54.9	45 32 59.0	8.5	3.3	35	0.012	17	5	SB(rs)c	SDSS	146
IC 2574	10 28 23.5	68 24 43.7	13.2	5.4	50	0.036	4.0	9	SAB(s)m	recal	450
NGC 3265	10 31 06.8	28 47 47.0	1.3	1.0	73	0.024	20	−5	E	$\cdots$	12
MRK 33	10 32 31.9	54 24 03.7	1.0	0.9	360	0.012	24	10	Im pec	recal	9
NGC 3351	10 43 57.7	11 42 13.0	7.4	5.0	13	0.028	12	3	SB(r)b	SDSS	176
NGC 3521	11 05 48.6	−00 02 09.1	11.0	5.1	343	0.058	9.0	4	SAB(rs)bc	SDSS	157
NGC 3621	11 18 16.5	−32 48 50.6	12.3	7.1	339	0.080	8.3	7	SA(s)d	recal	147
NGC 3627	11 20 15.0	12 59 29.6	9.1	4.2	353	0.032	9.1	3	SAB(s)b	SDSS	178
NGC 3773	11 38 13.0	12 06 42.9	1.2	1.0	345	0.027	13	−2	SA0	recal	31
NGC 3938	11 52 49.4	44 07 14.6	5.4	4.9	15	0.021	12	5	SA(s)c	SDSS	128
NGC 4125	12 08 06.0	65 10 26.9	5.8	3.2	275	0.019	21	−5	E6 pec	SDSS	102
NGC 4236	12 16 42.1	69 27 45.3	21.9	7.2	342	0.015	4.5	8	SB(s)dm	recal	571

Table 1—Continued

| Object name | RA$_{2000}$ | DEC$_{2000}$ | 2a | 2b | P.A. | E(B−V) | dist | T | Morphological | Optical | r_P |
| | (h:m:s) | (d:m:s) | (arcmin) | (arcmin) | (deg) | (mag) | (Mpc) | type | type | data | (arcsec) |
(1)	(2)	(3)	(4)	(5)	(6)	(7)	(8)	(9)	(10)	(11)	(12)
NGC 4254	12 18 49.6	14 24 59.4	5.4	4.7	35	0.039	17	5	SA(s)c	SDSS	128
NGC 4321	12 22 54.9	15 49 20.6	7.4	6.3	30	0.026	18	4	SAB(s)bc	SDSS	183
NGC 4450	12 28 29.6	17 05 05.8	5.2	3.9	355	0.028	17	2	SA(s)ab	SDSS	123
NGC 4536	12 34 27.1	02 11 16.4	7.6	3.2	310	0.018	15	4	SAB(rs)bc	SDSS	127
NGC 4552	12 35 39.8	12 33 22.8	5.1	4.7	360	0.041	15	−5	E0	SDSS	51
NGC 4559	12 35 57.7	27 57 35.1	10.7	4.4	330	0.018	17	6	SAB(rs)cd	SDSS	197
NGC 4569	12 36 49.8	13 09 46.3	9.5	4.4	23	0.046	17	2	SAB(rs)ab	SDSS	161
NGC 4579	12 37 43.6	11 49 05.1	5.9	4.7	275	0.041	17	3	SAB(rs)b	SDSS	135
NGC 4594	12 39 59.4	−11 37 23.0	8.7	3.5	90	0.051	9.1	1	SA(s)a	recal	212
NGC 4625	12 41 52.7	41 16 25.4	2.2	1.9	330	0.018	9.5	9	SAB(rs)m pec	SDSS	45
NGC 4631	12 42 08.0	32 32 29.4	15.5	2.7	86	0.017	9.0	7	SB(s)d	SDSS	266
NGC 4725	12 50 26.6	25 30 02.7	10.7	7.6	35	0.012	17	2	SAB(r)ab pec	SDSS	182
NGC 4736	12 50 53.1	41 07 13.6	11.2	9.1	285	0.018	5.2	2	(R)SA(r)ab	SDSS	60
DDO 154	12 54 05.3	27 08 58.7	3.0	2.2	35	0.009	4.3	10	IB(s)m	· · ·	78
NGC 4826	12 56 43.8	21 40 51.9	10.0	5.4	295	0.041	17	2	(R)SA(rs)ab	SDSS	177
DDO 165	13 06 24.9	67 42 25.0	3.5	1.9	90	0.024	4.6	10	Im	· · ·	156
NGC 5033	13 13 27.5	36 35 38.0	10.7	5.0	170	0.011	13	5	SA(s)c	SDSS	56
NGC 5055	13 15 49.3	42 01 45.4	12.6	7.2	285	0.018	8.2	4	SA(rs)bc	SDSS	231
NGC 5194 †	13 29 52.7	47 11 42.6	11.2	9.0	360	0.035	8.4	4	SA(s)bc pec	SDSS	222
NGC 5195	13 29 59.6	47 15 58.1	5.8	4.6	79	0.036	8.4	90	SB0 pec	SDSS	76
TOL 89	14 01 21.6	−33 03 49.6	2.8	1.7	352	0.066	16	8.1	(R')SB(s)dm pec	· · ·	89
NGC 5408	14 03 20.9	−41 22 40.0	1.6	0.8	12	0.069	4.5	9.7	IB(s)m	· · ·	· · ·
NGC 5474	14 05 01.6	53 39 44.0	4.8	4.3	360	0.011	6.8	6	SA(s)cd pec	SDSS	128
NGC 5713	14 40 11.5	−00 17 21.2	2.8	2.5	10	0.039	27	4	SAB(rs)bc pec	recal	43
NGC 5866	15 06 29.6	55 45 47.9	4.7	1.9	308	0.013	15	−1	SA0	SDSS	60
IC 4710	18 28 38.0	−66 58 56.0	3.6	2.8	5	0.089	8.5	9	SB(s)m	· · ·	141
NGC 6822	19 44 56.6	−14 47 21.4	15.5	13.5	7	0.236	0.60	10	IB(s)m	· · ·	448 (B)
NGC 6946	20 34 52.3	60 09 14.2	11.5	9.8	75	0.342	5.5	6	SAB(rs)cd	· · ·	286
NGC 7331	22 37 04.1	34 24 56.3	10.5	3.7	351	0.091	15	3	SA(s)b	recal	120
NGC 7552	23 16 10.8	−42 35 05.4	3.4	2.7	1	0.014	22	2	(R')SB(s)ab	recal	45
NGC 7793	23 57 49.8	−32 35 27.7	9.3	6.3	278	0.019	2.0	7	SA(s)d	· · ·	236

Note. — Sample. (1): Galaxy name. (2): RA(J2000) of the galaxy center. (3): DEC(J2000) of the galaxy center. (4),(5): Apparent major and minor isophotal diameters at μ_B=25 mag arcsec^{-2} from the RC3 catalog. (6): Position angle from RC3. †The PA and axis ratio for NGC 5194 differ from those in the RC3, which are affected by the presence of NGC 5195. (7): Galactic color excess from Schlegel et al. (1998). (8): Distance to the galaxy, rounded to the nearest Mpc when larger than 10 Mpc, taken from Gil de Paz et al. (2007) and Kennicutt et al. (2003). (9): Morphological type T as given in the RC3 catalog. (10): Full description of the morphological type from the RC3. (11): Optical data used for each galaxy: from the Sloan Digital Sky Survey (SDSS) or recalibrated with compiled aperture photometry (recal, see Section 2.2 and Appendix A). Galaxies lacking any label in this column have optical images with unreliable zero-points. Neither surface-brightness profiles nor asymptotic magnitudes are provided for these galaxies in the optical bands. However, we do provide morphological estimators, since they are not affected by zero-point errors. (12): Petrosian radius at $\eta = 0.2$, measured on the 3.6 μm images (except for a few galaxies where no meaningful solution was found, and the B-band images were used instead).

Table 2.   UV, optical and nIR surface photometry.

r	r	FUV 0.153 μm (mag/□)	NUV 0.227 μm (mag/□)	B 0.45 μm (mag/□)	V 0.55 μm (mag/□)	R 0.66 μm (mag/□)	I 0.81 μm (mag/□)	J 1.25 μm (mag/□)	H 1.65 μm (mag/□)	K_S 2.17 μm (mag/□)
(arcsec)	(kpc)									
					NGC 7331					
6	0.4	25.03±0.05	22.87±0.01	17.69±0.01	16.82±0.01	16.21±0.01	15.92±0.01	15.44±0.01	15.19±0.01	15.38±0.01
12	0.9	25.21±0.06	23.15±0.01	18.54±0.01	17.75±0.01	17.17±0.01	16.87±0.01	16.28±0.01	16.03±0.01	16.24±0.01
18	1.3	24.75±0.04	23.07±0.01	19.06±0.01	18.32±0.01	17.74±0.01	17.45±0.01	16.81±0.01	16.56±0.01	16.77±0.01
24	1.7	24.32±0.03	22.91±0.01	19.41±0.01	18.72±0.01	18.15±0.01	17.87±0.01	17.16±0.01	16.91±0.01	17.10±0.01
30	2.2	24.34±0.02	22.99±0.01	19.67±0.01	19.05±0.01	18.50±0.01	18.23±0.01	17.46±0.01	17.18±0.01	17.34±0.01
36	2.6	24.68±0.02	23.33±0.01	19.99±0.01	19.36±0.01	18.81±0.01	18.52±0.01	17.77±0.01	17.45±0.01	17.59±0.01

Note. — Surface photometry in the UV, optical and near-IR passbands for those SINGS galaxies lacking SDSS data. Only one sample galaxy is shown in the printed version, check the online edition for the full table. Radius is measured along the semimajor axis. The surface brightness is expressed in AB mag/arcsec^2. All values are corrected for foreground galactic extinction. The quoted uncertainties include photometric and sky errors, but not zero-point errors (see Section 3.2 for details). The optical values (columns 5 through 8) have been recalibrated to correct zero-point offsets present in the original data (see Section A). Again, the errors quoted here do not include the uncertainty resulting from the recalibration procedure.

Table 3. UV, optical (SDSS) and nIR surface photometry

r	r	FUV 0.153 μm	NUV 0.227 μm	u 0.354 μm	g 0.477 μm	r 0.623 μm	i 0.762 μm	z 0.913 μm	J 1.25 μm	H 1.65 μm	K_S 2.17 μm
(arcsec)	(kpc)	(mag/□)	(mag/□)	(mag/□)	(mag/□)	(mag/□)	(mag/□)	(mag/□)	(mag/□)	(mag/□)	(mag/□)
					NGC 3184						
6	0.3	24.15±0.12	23.25±0.05	22.03±0.02	20.55±0.01	19.81±0.01	19.41±0.01	19.17±0.01	18.79±0.01	18.58±0.01	18.83±0.02
12	0.5	25.52±0.21	24.85±0.10	22.73±0.03	21.14±0.01	20.40±0.01	19.99±0.01	19.80±0.01	19.44±0.01	19.29±0.02	19.55±0.02
18	0.8	25.57±0.12	24.77±0.05	22.92±0.04	21.39±0.01	20.69±0.01	20.30±0.01	20.12±0.01	19.78±0.01	19.60±0.02	19.85±0.02
24	1.0	24.83±0.07	24.16±0.03	22.83±0.04	21.48±0.01	20.85±0.01	20.49±0.01	20.32±0.01	19.97±0.01	19.81±0.02	20.04±0.02
30	1.3	24.38±0.05	23.97±0.03	22.84±0.04	21.61±0.01	21.03±0.01	20.69±0.01	20.53±0.02	20.20±0.02	20.00±0.02	20.29±0.03
36	1.5	24.70±0.05	24.22±0.03	23.16±0.05	21.89±0.01	21.29±0.01	20.95±0.01	20.79±0.02	20.48±0.02	20.30±0.02	20.58±0.03

Note. — Surface photometry in the UV, optical and near-IR passbands for those SINGS galaxies having SDSS data. Only one sample galaxy is shown in the printed version, check the online edition for the full table. The radius is measured along the semimajor axis. The surface brightness is in AB (mag/arcsec^2). All values are corrected for foreground galactic extinction. The quoted uncertainties include photometric and sky errors, but not zero-point errors (see Section 3.2 for details).

Table 4.   IRAC and MIPS surface photometry

r (arcsec)	r (kpc)	$\log I_{3.6\mu m}$ (Jy/□)	$\log I_{4.5\mu m}$ (Jy/□)	$\log I_{5.8\mu m}$ (Jy/□)	$\log I_{8.0\mu m}$ (Jy/□)	$\log I_{24\mu m}$ (Jy/□)	$\log I_{70\mu m}$ (Jy/□)	$\log I_{160\mu m}$ (Jy/□)
				NGC 3184				
6	0.3	-4.28±0.01	-4.46±0.01	-4.29±0.01	-3.97±0.01	-3.60±0.01		
12	0.5	-4.58±0.01	-4.77±0.01	-4.74±0.01	-4.54±0.01	-4.14±0.01	-3.06±0.01	-2.75±0.01
18	0.8	-4.72±0.01	-4.90±0.01	-4.81±0.01	-4.57±0.01	-4.52±0.01		
24	1.0	-4.77±0.01	-4.96±0.01	-4.77±0.01	-4.45±0.01	-4.49±0.01	-3.39±0.02	-2.82±0.01
30	1.3	-4.86±0.01	-5.04±0.01	-4.83±0.01	-4.49±0.01	-4.52±0.01		
36	1.5	-4.96±0.01	-5.15±0.01	-4.94±0.01	-4.61±0.01	-4.62±0.01	-3.47±0.02	-2.88±0.01

Note. — Surface photometry in the IRAC and MIPS bands. Check the online edition for the full table with all galaxies. The radius is measured along the semimajor axis. The surface brightness is in Jy/arcsec^2. All values are corrected for foreground galactic extinction. The quoted uncertainties include photometric and sky errors, but not zero-point errors (see Section 3.2 for details).

Table 5.   UV, optical and nIR asymptotic magnitudes.

Galaxy	FUV 0.153 μm (mag)	NUV 0.227 μm (mag)	B 0.45 μm (mag)	V 0.55 μm (mag)	R 0.66 μm (mag)	I 0.81 μm (mag)	J 1.25 μm (mag)	H 1.65 μm (mag)	K_S 2.17 μm (mag)
				Galaxies with recalibrated optical data					
NGC 0024	14.039±0.004	13.757±0.003	11.912±0.002	11.341±0.002	11.276±0.002	10.553±0.002	10.501±0.006	10.371±0.011	10.714±0.010
NGC 0584	17.506±0.059	15.631±0.015	11.506±0.003	10.491±0.003	10.194±0.004	9.759±0.004	9.065±0.005	8.758±0.009	9.099±0.009
NGC 0925	12.072±0.001	11.852±0.001	10.471±0.003	9.972±0.003	· · ·	9.648±0.006	9.464±0.002	9.310±0.007	9.604±0.005
NGC 1097	12.542±0.004	12.167±0.003	9.860±0.001	9.300±0.001	8.958±0.001	8.623±0.001	8.019±0.001	7.825±0.002	8.050±0.003
NGC 1291	14.229±0.015	13.380±0.005	9.439±0.001	8.675±0.002	8.282±0.003	7.925±0.005	7.374±0.001	7.305±0.003	7.444±0.001
NGC 1316	15.071±0.056	13.079±0.026	9.080±0.014	8.353±0.008	7.968±0.010	7.709±0.005	7.438±0.001	7.373±0.001	7.547±0.001
NGC 1377	· · ·	· · ·	13.041±0.010	12.679±0.008	12.326±0.006	12.007±0.008	11.468±0.004	11.274±0.015	11.515±0.013
NGC 1404	16.413±0.008	15.275±0.013	10.763±0.011	9.988±0.010	9.598±0.011	9.175±0.010	8.648±0.001	8.447±0.003	8.644±0.002
NGC 1482	17.456±0.006	16.279±0.020	12.974±0.021	12.307±0.011	· · ·	· · ·	10.539±0.008	10.246±0.004	10.266±0.010
NGC 1512	13.468±0.006	13.131±0.010	10.944±0.009	10.360±0.005	10.011±0.003	9.660±0.002	9.207±0.003	9.160±0.003	9.330±0.006
NGC 1566	12.046±0.011	11.830±0.010	10.006±0.004	9.438±0.001	9.271±0.002	9.045±0.001	8.601±0.003	8.577±0.003	8.716±0.004
NGC 1705	13.381±0.002	13.353±0.001	12.799±0.002	12.466±0.002	12.378±0.002	12.063±0.006	12.016±0.021	12.062±0.017	12.226±0.019
NGC 2798	16.525±0.003	15.698±0.003	13.028±0.013	12.380±0.010	· · ·	11.634±0.008	10.930±0.005	10.699±0.010	10.849±0.009
NGC 2915	13.339±0.005	13.309±0.004	· · ·	11.826±0.014	11.529±0.012	· · ·	11.057±0.026	10.823±0.029	11.290±0.040
IC 2574	12.143±0.002	12.113±0.001	11.029±0.002	10.705±0.004	· · ·	· · ·	10.421±0.024	12.913±0.397	11.754±0.035
MRK 33	14.854±0.003	14.607±0.002	13.858±0.001	13.270±0.001	· · ·	· · ·	12.073±0.030	11.856±0.056	12.026±0.074
NGC 3621	11.632±0.022	11.218±0.012	9.487±0.025	9.114±0.011	8.991±0.010	8.732±0.008	8.371±0.005	8.196±0.004	8.469±0.005
NGC 3773	14.836±0.008	14.539±0.008	13.479±0.005	13.167±0.008	· · ·	· · ·	12.247±0.023	12.406±0.037	12.485±0.044
NGC 4236	11.769±0.001	11.565±0.001	10.149±0.002	10.050±0.002	· · ·	· · ·	9.620±0.008	9.234±0.010	9.676±0.011
NGC 4594	14.501±0.013	13.221±0.008	8.997±0.001	8.128±0.002	7.424±0.001	6.925±0.001	6.717±0.001	6.536±0.001	6.774±0.001
NGC 5713	14.615±0.003	13.892±0.001	11.723±0.004	11.177±0.002	· · ·	10.485±0.002	10.047±0.004	9.977±0.009	10.171±0.003
NGC 7331	13.357±0.002	12.681±0.002	9.672±0.003	9.109±0.002	8.516±0.010	8.180±0.008	7.857±0.002	7.613±0.002	7.818±0.001
NGC 7552	14.196±0.002	13.474±0.001	11.079±0.005	10.516±0.010	· · ·	· · ·	9.342±0.001	9.183±0.002	9.341±0.002
				Galaxies without recalibrated optical data					
NGC 0337	13.781±0.001	13.156±0.001	· · ·	· · ·	· · ·	· · ·	10.749±0.005	10.670±0.009	10.923±0.006
NGC 0628	11.685±0.005	11.399±0.004	· · ·	· · ·	· · ·	· · ·	8.432±0.004	8.349±0.003	8.666±0.005
NGC 0855	15.924±0.006	15.224±0.005	· · ·	· · ·	· · ·	· · ·	11.452±0.011	11.328±0.022	11.561±0.013

Table 5—Continued

Galaxy	FUV 0.153 μm (mag)	NUV 0.227 μm (mag)	B 0.45 μm (mag)	V 0.55 μm (mag)	R 0.66 μm (mag)	I 0.81 μm (mag)	J 1.25 μm (mag)	H 1.65 μm (mag)	K_S 2.17 μm (mag)
NGC 1266	19.690±0.057	17.693±0.018	$\cdots$	$\cdots$	$\cdots$	$\cdots$	11.282±0.010	11.212±0.014	11.315±0.016
NGC 2403	10.315±0.002	10.111±0.002	$\cdots$	$\cdots$	$\cdots$	$\cdots$	7.841±0.001	7.770±0.002	8.048±0.003
Holmberg II	12.198±0.001	12.176±0.001	$\cdots$	$\cdots$	$\cdots$	$\cdots$	10.390±0.010	9.486±0.029	9.899±0.012
M81 Dwa	17.364±0.004	17.150±0.009	$\cdots$	$\cdots$	$\cdots$	$\cdots$	$\cdots$	$\cdots$	$\cdots$
DDO 053	15.311±0.003	15.336±0.002	$\cdots$	$\cdots$	$\cdots$	$\cdots$	$\cdots$	$\cdots$	$\cdots$
Holmberg I	14.606±0.010	14.543±0.012	$\cdots$	$\cdots$	$\cdots$	$\cdots$	$\cdots$	$\cdots$	$\cdots$
Holmberg IX	14.875±0.011	14.628±0.015	$\cdots$	$\cdots$	$\cdots$	$\cdots$	$\cdots$	$\cdots$	$\cdots$
M81 Dwb	16.626±0.009	16.394±0.007	$\cdots$	$\cdots$	$\cdots$	$\cdots$	$\cdots$	$\cdots$	$\cdots$
NGC 3265	16.983±0.006	16.405±0.008	$\cdots$	$\cdots$	$\cdots$	$\cdots$	12.198±0.004	12.037±0.003	12.234±0.009
DDO 154	14.721±0.004	14.757±0.006	$\cdots$	$\cdots$	$\cdots$	$\cdots$	14.166±0.099	$\cdots$	$\cdots$
DDO 165	14.317±0.003	14.104±0.002	$\cdots$	$\cdots$	$\cdots$	$\cdots$	12.961±0.070	$\cdots$	13.899±0.197
TOL 89	14.222±0.003	13.772±0.002	$\cdots$	$\cdots$	$\cdots$	$\cdots$	11.743±0.014	12.134±0.020	12.083±0.022
NGC 5408	$\cdots$	$\cdots$	$\cdots$	$\cdots$	$\cdots$	$\cdots$	11.907±0.048	11.643±0.036	12.144±0.063
IC 4710	13.723±0.002	13.379±0.024	$\cdots$	$\cdots$	$\cdots$	$\cdots$	11.294±0.014	11.765±0.016	11.792±0.017
NGC 6822	10.060±0.001	9.713±0.002	$\cdots$	$\cdots$	$\cdots$	$\cdots$	7.457±0.009	7.440±0.009	7.806±0.012
NGC 6946	10.425±0.003	9.741±0.002	$\cdots$	$\cdots$	$\cdots$	$\cdots$	6.831±0.015	7.076±0.013	7.072±0.011
NGC 7793	11.160±0.001	10.988±0.001	$\cdots$	$\cdots$	$\cdots$	$\cdots$	8.479±0.002	8.430±0.004	8.743±0.008

Note. — Asymptotic magnitudes in the UV, optical and near-IR passbands for those SINGS galaxies lacking SDSS data. All values are in AB magnitudes, and corrected for foreground galactic extinction. The quoted uncertainties are just the statitistical errors resulting from the fit applied to the growth curve, but do not include zero-point errors (see Section 4.1 for details). The optical values (columns 5 through 8) have been recalibrated to correct zero-point offsets present in the original data (see Section A). Again, the errors quoted here do not include the uncertainty resulting from the recalibration procedure.

Table 6.   UV, optical (SDSS) and nIR asymptotic magnitudes.

Galaxy	FUV 0.153 μm (mag)	NUV 0.227 μm (mag)	u 0.354 μm (mag)	g 0.477 μm (mag)	r 0.623 μm (mag)	i 0.762 μm (mag)	z 0.913 μm (mag)	J 1.25 μm (mag)	H 1.65 μm (mag)	K_S 2.17 μm (mag)
NGC 2841	13.527±0.019	13.014±0.010	11.229±0.003	9.696±0.001	8.953±0.001	8.515±0.001	8.269±0.001	7.910±0.001	7.687±0.001	7.934±0.001
NGC 2976	13.227±0.003	12.707±0.003	11.464±0.002	10.293±0.001	9.749±0.002	9.471±0.001	9.293±0.002	9.163±0.002	9.046±0.002	9.312±0.003
NGC 3049	$\cdots$	14.736±0.004	13.787±0.007	12.884±0.008	12.350±0.010	12.112±0.011	11.909±0.018	11.621±0.007	11.631±0.009	11.731±0.022
NGC 3031	10.744±0.002	10.344±0.002	8.640±0.004	7.177±0.002	6.487±0.001	6.068±0.001	5.861±0.001	5.601±0.001	5.411±0.001	5.632±0.001
NGC 3034	12.345±0.016	11.313±0.005	9.669±0.001	8.234±0.001	7.542±0.001	7.231±0.001	7.030±0.001	6.593±0.001	6.336±0.001	6.433±0.001
NGC 3190	17.372±0.012	15.803±0.008	12.842±0.008	11.317±0.002	10.545±0.001	10.136±0.001	9.885±0.002	9.360±0.001	9.110±0.002	9.272±0.001
NGC 3184	12.476±0.002	12.177±0.001	11.236±0.001	10.078±0.001	9.582±0.001	9.298±0.001	9.186±0.002	9.019±0.004	8.817±0.005	9.094±0.004
NGC 3198	12.985±0.002	12.777±0.001	11.600±0.017	10.714±0.006	10.283±0.004	10.001±0.004	9.808±0.006	9.584±0.004	9.397±0.006	9.603±0.004
NGC 3351	13.287±0.001	12.756±0.001	11.515±0.003	10.113±0.002	9.432±0.003	9.062±0.003	8.860±0.004	8.419±0.003	8.303±0.001	8.479±0.002
NGC 3521	12.943±0.003	12.222±0.002	10.473±0.004	9.042±0.002	8.416±0.002	8.056±0.001	7.853±0.002	7.564±0.001	7.340±0.001	7.570±0.002
NGC 3627	12.664±0.001	11.887±0.001	10.276±0.008	9.083±0.002	8.471±0.002	8.158±0.001	7.969±0.002	7.686±0.001	7.496±0.001	7.698±0.001
NGC 3938	$\cdots$	12.512±0.002	11.476±0.005	10.538±0.002	10.113±0.003	9.840±0.003	9.741±0.003	9.500±0.003	9.534±0.008	9.627±0.010
NGC 4125	$\cdots$	15.068±0.014	12.098±0.006	10.251±0.003	9.519±0.003	9.091±0.010	8.882±0.005	8.653±0.003	8.477±0.002	8.709±0.003
NGC 4254	$\cdots$	11.935±0.002	10.952±0.001	9.954±0.001	9.466±0.001	9.204±0.001	9.105±0.001	8.760±0.004	8.634±0.008	8.779±0.006
NGC 4321	$\cdots$	12.036±0.003	10.690±0.002	9.653±0.001	9.064±0.001	8.769±0.001	8.559±0.003	8.312±0.003	8.167±0.020	8.429±0.002
NGC 4450	$\cdots$	14.519±0.008	11.822±0.011	10.465±0.002	9.722±0.002	9.338±0.001	$\cdots$	8.799±0.002	8.542±0.002	8.868±0.004
NGC 4536	13.279±0.001	13.009±0.001	11.742±0.004	10.743±0.001	10.179±0.001	9.864±0.002	9.678±0.001	9.307±0.004	9.155±0.003	9.284±0.005
NGC 4552	15.648±0.026	14.692±0.009	12.035±0.004	10.287±0.005	9.503±0.004	9.083±0.004	8.864±0.004	8.460±0.002	8.271±0.002	8.545±0.002
NGC 4559	12.094±0.001	11.879±0.001	11.107±0.002	10.130±0.001	9.740±0.001	9.517±0.003	9.372±0.005	9.307±0.001	9.209±0.003	9.431±0.002
NGC 4569	14.456±0.004	13.176±0.001	11.147±0.004	9.764±0.003	9.246±0.003	8.885±0.003	8.756±0.003	8.367±0.002	8.141±0.002	8.422±0.002
NGC 4579	14.438±0.006	13.657±0.002	11.449±0.002	9.931±0.001	9.226±0.001	8.816±0.001	8.643±0.001	8.273±0.004	8.046±0.003	8.319±0.002
NGC 4625	14.506±0.009	14.166±0.005	13.824±0.003	12.720±0.003	12.189±0.002	11.947±0.002	11.815±0.002	11.498±0.012	11.284±0.011	11.612±0.005
NGC 4631	11.321±0.001	11.086±0.001	10.229±0.002	9.441±0.001	9.048±0.001	8.802±0.001	8.827±0.001	8.380±0.001	8.219±0.001	8.307±0.002
NGC 4725	12.989±0.005	12.660±0.005	11.166±0.001	9.605±0.001	8.928±0.001	8.530±0.001	8.499±0.008	8.089±0.003	7.695±0.004	8.039±0.003
NGC 4736	11.777±0.004	11.353±0.014	9.759±0.005	8.344±0.002	7.681±0.001	7.348±0.001	7.214±0.001	6.944±0.001	6.737±0.002	6.969±0.001
NGC 4826	13.453±0.001	12.439±0.001	10.193±0.001	8.770±0.001	8.114±0.001	7.733±0.001	7.538±0.002	7.136±0.001	6.940±0.001	7.171±0.001
NGC 5033	13.237±0.001	12.968±0.001	11.670±0.001	10.406±0.001	9.802±0.001	9.450±0.003	9.203±0.009	8.762±0.002	8.567±0.006	8.770±0.007
NGC 5055	12.353±0.003	11.815±0.002	10.080±0.001	8.877±0.001	8.213±0.001	7.842±0.001	7.660±0.001	7.469±0.002	7.215±0.003	7.449±0.003
NGC 5194	11.006±0.002	10.490±0.001	9.594±0.001	8.495±0.001	7.989±0.001	7.699±0.001	7.546±0.001	7.279±0.001	7.033±0.002	7.311±0.002
NGC 5195	14.935±0.055	13.845±0.008	10.950±0.004	9.611±0.009	8.893±0.014	8.446±0.015	8.346±0.017	8.081±0.002	7.826±0.004	8.072±0.003
NGC 5474	12.932±0.001	12.805±0.001	12.231±0.002	11.229±0.018	10.845±0.007	10.617±0.005	10.558±0.001	10.456±0.005	10.143±0.015	10.667±0.011
NGC 5866	16.807±0.012	14.814±0.006	11.999±0.002	10.372±0.002	9.662±0.002	9.252±0.002	9.055±0.004	8.701±0.002	8.480±0.002	8.686±0.004

Note. — Asymptotic magnitudes in the UV, optical and near-IR passbands for those SINGS galaxies with available SDSS data. All values are in AB magnitudes, and are corrected for foreground galactic extinction. The quoted uncertainties are just the statitistical errors resulting from the fit applied to the growth curve, but do not include zero-point errors (see Section 4.1 for details).

Table 7.   IRAC and MIPS asymptotic magnitudes.

Galaxy	$\log F_{3.6\mu m}$ (Jy)	$\log F_{4.5\mu m}$ (Jy)	$\log F_{5.8\mu m}$ (Jy)	$\log F_{8.0\mu m}$ (Jy)	$\log F_{24\mu m}$ (Jy)	$\log F_{70\mu m}$ (Jy)	$\log F_{160\mu m}$ (Jy)
NGC 0024	-0.984±0.001	-1.153±0.002	-1.169±0.002	-0.936±0.001	-0.904±0.004	0.362±0.005	0.825±0.024
NGC 0337	-1.006±0.001	-1.164±0.002	-0.810±0.001	-0.430±0.001	-0.146±0.004	1.006±0.002	1.279±0.009
NGC 0584	-0.450±0.001	-0.661±0.001	-0.850±0.001	-1.051±0.001	-1.380±0.008	-0.538±0.060	$\cdots$
NGC 0628	-0.076±0.002	-0.241±0.002	0.046±0.002	0.461±0.002	0.498±0.003	1.536±0.002	2.087±0.001
NGC 0855	-1.371±0.003	-1.544±0.002	-1.493±0.004	-1.356±0.002	-1.132±0.006	0.186±0.009	0.366±0.015
NGC 0925	-0.494±0.002	-0.656±0.002	-0.508±0.003	-0.158±0.003	-0.046±0.007	1.158±0.005	1.621±0.002
NGC 1097	0.089±0.001	-0.084±0.001	0.147±0.006	0.504±0.006	0.816±0.002	1.737±0.002	2.165±0.001
NGC 1266	-1.269±0.002	-1.377±0.002	-1.271±0.011	-1.053±0.008	-0.074±0.004	1.013±0.005	0.802±0.010
NGC 1291	0.308±0.001	0.104±0.001	-0.080±0.001	-0.178±0.001	-0.288±0.004	0.808±0.030	1.458±0.001
NGC 1316	0.428±0.003	0.228±0.004	0.057±0.003	-0.147±0.001	-0.337±0.011	0.734±0.011	1.059±0.003
NGC 1377	-1.262±0.003	-1.066±0.002	-0.497±0.001	-0.366±0.001	0.219±0.006	0.735±0.015	0.301±0.011
NGC 1404	-0.188±0.003	-0.396±0.004	-0.550±0.002	-0.789±0.004	-1.241±0.014	$\cdots$	$\cdots$
NGC 1482	-0.696±0.004	-0.827±0.003	-0.254±0.001	0.186±0.001	0.553±0.004	1.397±0.006	1.548±0.005
NGC 1512	-0.382±0.004	-0.589±0.006	-0.561±0.004	-0.361±0.001	-0.320±0.003	0.818±0.005	1.404±0.004
NGC 1566	-0.123±0.004	-0.285±0.004	-0.072±0.002	0.312±0.002	0.436±0.002	1.514±0.002	1.998±0.001
NGC 1705	-1.564±0.002	-1.696±0.003	-1.836±0.001	-1.745±0.002	-1.278±0.007	0.104±0.003	0.219±0.004
NGC 2403	0.244±0.001	0.074±0.001	0.287±0.001	0.611±0.001	0.768±0.001	1.938±0.001	2.386±0.001
Holmberg II	-1.151±0.003	-1.250±0.006	-1.514±0.002	-1.252±0.012	-0.698±0.010	0.614±0.010	0.711±0.020
M81 Dwa	-2.563±0.095	-2.935±0.048	$\cdots$	$\cdots$	$\cdots$	$\cdots$	$\cdots$
DDO 053	-2.145±0.017	-2.144±0.018	-2.746±0.033	-2.489±0.022	-1.563±0.040	-0.396±0.007	-0.213±0.040
NGC 2798	-1.160±0.002	-1.330±0.001	-0.650±0.001	-0.235±0.001	0.405±0.003	1.232±0.004	1.207±0.019
NGC 2841	0.090±0.001	-0.121±0.001	-0.191±0.001	0.035±0.001	-0.045±0.001	0.990±0.001	1.772±0.002
NGC 2915	-1.280±0.005	-1.447±0.004	-1.584±0.003	-1.561±0.002	-1.240±0.003	0.088±0.007	0.036±0.044
Holmberg I	-1.924±0.010	-2.112±0.011	$\cdots$	-2.085±0.028	$\cdots$	-0.449±0.005	-0.092±0.016
NGC 2976	-0.389±0.001	-0.556±0.001	-0.315±0.001	-0.002±0.001	0.139±0.001	1.293±0.002	1.702±0.006
NGC 3049	-1.386±0.001	-1.562±0.001	-1.263±0.002	-0.889±0.029	-0.377±0.003	0.416±0.010	0.640±0.030
NGC 3031	1.023±0.001	0.819±0.001	0.745±0.001	0.881±0.001	0.704±0.001	1.924±0.001	2.562±0.002
NGC 3034	$\cdots$	$\cdots$	$\cdots$	$\cdots$	$\cdots$	$\cdots$	$\cdots$
Holmberg IX	-1.596±0.101	-1.795±0.110	$\cdots$	$\cdots$	$\cdots$	$\cdots$	$\cdots$
M81 Dwb	-2.237±0.015	-2.386±0.013	-2.724±0.014	-2.439±0.021	-2.121±0.050	-0.808±0.025	$\cdots$
NGC 3190	-0.451±0.001	-0.651±0.001	-0.680±0.001	-0.532±0.001	-0.587±0.002	0.700±0.003	1.158±0.026
NGC 3184	-0.288±0.001	-0.473±0.001	-0.235±0.001	0.143±0.001	0.152±0.001	1.199±0.001	1.834±0.001
NGC 3198	-0.569±0.001	-0.750±0.001	-0.602±0.001	-0.170±0.001	0.017±0.001	0.996±0.002	1.575±0.002
IC 2574	-0.780±0.009	-0.847±0.013	-1.257±0.010	-1.129±0.034	-0.547±0.006	0.739±0.002	1.054±0.007
NGC 3265	-1.596±0.002	-1.762±0.002	-1.420±0.002	-1.011±0.013	-0.577±0.009	0.380±0.014	0.335±0.022
MRK 33	-1.584±0.003	-1.711±0.004	-1.311±0.006	-0.894±0.001	-0.073±0.005	0.582±0.002	0.686±0.081
NGC 3351	-0.112±0.001	-0.298±0.001	-0.184±0.001	0.098±0.001	0.401±0.002	1.316±0.001	1.795±0.001
NGC 3521	0.291±0.001	0.112±0.001	0.363±0.001	0.740±0.001	0.735±0.001	1.763±0.003	2.345±0.002
NGC 3621	-0.001±0.002	-0.176±0.002	0.161±0.001	0.529±0.001	0.546±0.002	1.667±0.001	2.121±0.001
NGC 3627	0.252±0.001	0.079±0.001	0.330±0.001	0.707±0.001	0.866±0.001	1.916±0.001	2.338±0.002
NGC 3773	-1.654±0.006	-1.850±0.004	-1.632±0.001	-1.328±0.002	-0.885±0.010	0.170±0.004	0.390±0.042
NGC 3938	-0.502±0.001	-0.676±0.001	-0.384±0.003	-0.009±0.004	0.032±0.004	1.138±0.001	1.688±0.001
NGC 4125	-0.164±0.002	-0.372±0.002	-0.520±0.002	-0.762±0.002	-1.021±0.011	0.004±0.008	0.137±0.001
NGC 4236	-0.524±0.004	-0.670±0.004	-0.970±0.012	-0.604±0.010	-0.248±0.006	0.940±0.002	1.338±0.002
NGC 4254	-0.161±0.001	-0.324±0.001	0.153±0.001	0.588±0.001	0.622±0.001	1.667±0.001	2.134±0.001

Table 7—Continued

Galaxy	$\log F_{3.6\mu m}$ (Jy)	$\log F_{4.5\mu m}$ (Jy)	$\log F_{5.8\mu m}$ (Jy)	$\log F_{8.0\mu m}$ (Jy)	$\log F_{24\mu m}$ (Jy)	$\log F_{70\mu m}$ (Jy)	$\log F_{160\mu m}$ (Jy)
NGC 4321	-0.022±0.001	-0.191±0.002	0.060±0.001	0.465±0.001	0.524±0.001	1.589±0.002	2.134±0.002
NGC 4450	-0.284±0.001	-0.477±0.001	-0.585±0.001	-0.587±0.002	-0.704±0.002	0.457±0.005	1.182±0.004
NGC 4536	-0.379±0.003	-0.536±0.003	-0.185±0.004	0.196±0.004	0.543±0.002	1.450±0.002	1.739±0.002
NGC 4552	-0.087±0.003	-0.313±0.002	-0.504±0.001	-0.678±0.002	-1.021±0.010	-1.451±3.537	⋯
NGC 4559	-0.433±0.001	-0.598±0.002	-0.407±0.001	-0.067±0.001	0.038±0.001	1.227±0.001	1.721±0.002
NGC 4569	-0.123±0.001	-0.308±0.001	-0.245±0.001	0.006±0.001	0.153±0.001	1.065±0.003	1.583±0.001
NGC 4579	-0.064±0.001	-0.267±0.001	-0.287±0.001	-0.132±0.001	-0.110±0.001	0.977±0.005	1.594±0.001
NGC 4594	0.589±0.001	0.375±0.001	0.211±0.001	0.100±0.001	-0.166±0.001	0.868±0.001	1.584±0.003
NGC 4625	-1.304±0.007	-1.453±0.023	-1.262±0.003	-0.875±0.004	-0.874±0.004	0.327±0.007	0.731±0.005
NGC 4631	0.077±0.001	-0.067±0.001	0.354±0.001	0.755±0.001	0.900±0.001	2.054±0.001	2.420±0.006
NGC 4725	0.037±0.001	-0.172±0.001	-0.182±0.002	0.050±0.002	-0.079±0.002	0.926±0.001	1.750±0.001
NGC 4736	0.563±0.002	0.356±0.002	0.382±0.001	0.692±0.001	0.752±0.003	1.919±0.001	2.250±0.001
DDO 154	-2.217±0.023	-2.232±0.028	⋯	⋯	⋯	⋯	⋯
NGC 4826	0.384±0.001	0.189±0.001	0.174±0.001	0.338±0.001	0.400±0.001	1.642±0.002	1.945±0.002
DDO 165	-1.794±0.006	-1.916±0.006	-1.856±0.064	⋯	⋯	⋯	⋯
NGC 5033	-0.188±0.001	-0.360±0.001	-0.095±0.006	0.289±0.001	0.298±0.004	1.392±0.002	1.948±0.001
NGC 5055	0.379±0.001	0.204±0.001	0.401±0.001	0.761±0.001	0.755±0.001	1.838±0.001	2.487±0.001
NGC 5194	0.416±0.001	0.245±0.001	0.599±0.001	1.018±0.001	1.080±0.001	2.119±0.001	2.681±0.001
NGC 5195	0.066±0.002	-0.130±0.001	-0.193±0.001	0.066±0.008	0.220±0.004	1.298±0.004	1.736±0.011
TOL 89	-1.378±0.002	-1.538±0.002	-1.518±0.006	-1.228±0.004	-0.587±0.003	0.262±0.008	0.556±0.020
NGC 5408	-1.520±0.019	-1.741±0.011	-1.789±0.040	-1.620±0.056	-0.408±0.001	0.678±0.140	0.430±0.097
NGC 5474	-0.981±0.001	-1.161±0.001	-1.268±0.014	-0.958±0.001	-0.714±0.008	0.563±0.002	1.022±0.003
NGC 5713	-0.699±0.001	-0.851±0.001	-0.381±0.001	0.050±0.001	0.364±0.002	1.296±0.006	1.577±0.008
NGC 5866	-0.187±0.001	-0.387±0.001	-0.520±0.001	-0.538±0.001	-0.674±0.002	0.900±0.002	1.208±0.002
IC 4710	-1.187±0.002	-1.354±0.002	-1.410±0.005	-1.292±0.005	-0.966±0.003	0.342±0.001	0.462±0.006
NGC 6822	0.489±0.013	0.256±0.008	0.241±0.011	0.199±0.006	0.516±0.008	1.832±0.004	2.158±0.003
NGC 6946	0.517±0.001	0.336±0.001	0.747±0.001	1.160±0.001	1.306±0.001	2.289±0.001	2.695±0.001
NGC 7331	0.199±0.001	0.019±0.001	0.247±0.001	0.607±0.001	0.608±0.001	1.825±0.002	2.232±0.002
NGC 7552	-0.356±0.003	-0.453±0.002	-0.025±0.002	0.394±0.002	1.018±0.001	1.732±0.004	1.912±0.003
NGC 7793	-0.127±0.001	-0.299±0.001	-0.048±0.001	0.282±0.001	0.311±0.001	1.526±0.001	2.071±0.001

Note. — Asymptotic fluxes F_ν in the IRAC and MIPS bands. All values are in Jy, and are corrected for foreground galactic extinction. The quoted uncertainties are just the statitistical errors resulting from the fit applied to the growth curve, but do not include zero-point errors (see Section 4.1 for details).

Table 8. Non-parametrical morphological estimators.

Galaxy		FUV	NUV	B	V	R	I	u	g	r	i	z	J	H	K_S	3.6 μm	4.5 μm	5.8 μm	8.0 μm	24 μm	70 μm	160 μm
NGC 0925	C_{42}	2.55	2.63	2.84	2.90	2.99	3.14	$\cdots$	$\cdots$	$\cdots$	$\cdots$	$\cdots$	3.07	3.02	3.05	3.27	3.25	3.40	3.51	3.14	3.01	2.52
SAB(s)d	A	0.404	0.350	0.176	0.109	0.133	0.095	$\cdots$	$\cdots$	$\cdots$	$\cdots$	$\cdots$	0.015	0.010	0.000	0.149	0.123	0.134	0.260	0.309	0.224†	0.205†
$T = 7$	G	0.648	0.619	0.551	0.516	0.550	0.530	$\cdots$	$\cdots$	$\cdots$	$\cdots$	$\cdots$	0.516	0.482	0.467	0.600	0.599	0.616	0.676	0.692	0.615†	0.509†
	$\overline{M}_{20}$	−0.90	−0.95	−1.21	−1.41	−1.42	−1.64	$\cdots$	$\cdots$	$\cdots$	$\cdots$	$\cdots$	−1.75	−1.75	−1.58	−1.56	−1.41	−1.27	−1.28	−0.85	−1.15†	−1.62†
NGC 2841	C_{42}	2.28	2.36	3.77	3.93	3.93	3.89	3.33	3.84	3.92	3.91	3.96	3.84	3.84	3.84	3.95	3.83	3.12	2.00	1.82	1.90	2.15
SA(r)b	A	0.289	0.213	0.107	0.082	0.065	0.052	0.084	0.098	0.070	0.054	0.031	0.009	0.008	0.000	0.027	0.018	0.022	0.086	0.084	0.041†	0.081†
$T = 3$	G	0.586	0.586	0.595	0.606	0.610	0.605	0.566	0.611	0.626	0.629	0.647	0.666	0.662	0.667	0.648	0.645	0.633	0.601	0.612	0.610†	0.444†
	$\overline{M}_{20}$	−1.02	−1.15	−2.42	−2.47	−2.45	−2.51	−2.16	−2.48	−2.53	−2.55	−2.61	−2.58	−2.55	−2.57	−2.56	−2.54	−2.03	−1.09	−0.99	−1.02†	−1.04†
NGC 3190	C_{42}	2.95	3.16	3.70	3.99	4.20	4.14	3.90	4.00	4.15	4.13	4.11	4.12	4.10	4.21	4.44	4.40	4.11	3.85	3.62	2.93	3.05
SA(s)a pec	A	0.171†	0.226†	0.260	0.213	0.180	0.148	0.178	0.247	0.211	0.172	0.119	0.062	0.052	0.043	0.080	0.064	0.073	0.131	0.160	0.202†	0.227†
$T = 1$	G	0.486†	0.592†	0.675	0.693	0.701	0.714	0.621	0.688	0.710	0.723	0.746	0.758	0.769	0.762	0.773	0.769	0.755	0.808	0.788	0.706†	0.479†
	$\overline{M}_{20}$	−1.58†	−1.92†	−2.67	−2.73	−2.71	−2.70	−2.45	−2.74	−2.73	−2.77	−2.80	−2.77	−2.57	−2.68	−2.75	−2.58	−2.54	−2.00	−2.28	−2.07†	−1.69†
NGC 3184	C_{42}	1.73	1.78	2.22	2.35	2.44	2.56	2.03	2.27	2.41	2.51	2.56	2.62	2.70	2.63	2.55	2.51	2.03	1.89	2.06	2.05	2.12
SAB(rs)cd	A	0.537	0.400	0.163	0.104	0.093	0.068	0.153	0.143	0.121	0.089	0.042	0.026	0.011	0.008	0.137	0.125	0.186	0.293	0.294	0.200†	0.085†
$T = 6$	G	0.771	0.598	0.490	0.492	0.513	0.520	0.509	0.510	0.525	0.531	0.532	0.518	0.496	0.483	0.553	0.562	0.591	0.640	0.662	0.592†	0.486†
	$\overline{M}_{20}$	−0.84	−0.90	−1.26	−1.43	−1.50	−1.62	−0.94	−1.31	−1.45	−1.59	−1.62	−1.73	−1.72	−1.60	−1.47	−1.39	−0.98	−0.94	−0.98	−1.14†	−1.45†
NGC 4125	C_{42}	$\cdots$	4.48	4.12	4.30	4.34	4.32	4.21	4.63	4.71	4.75	4.78	4.40	4.38	4.36	5.17	5.10	5.00	5.10	5.18	> 2.92	> 1.86
E6 pec	A	$\cdots$ †	0.104†	0.106	0.098	0.087	0.172	0.000	0.016	0.015	0.011	0.000	0.030	0.023	0.025	0.036	0.033	0.000	0.000	0.025†	0.108†	0.162†
$T = -5$	G	$\cdots$ †	0.610†	0.713	0.701	0.712	0.723	0.629	0.659	0.672	0.672	0.696	0.727	0.726	0.711	0.686	0.684	0.650	0.696	0.652†	0.741†	0.625†
	$\overline{M}_{20}$	$\cdots$ †	−2.32†	−2.52	−2.58	−2.60	−1.56	−2.47	−2.55	−2.60	−2.59	−2.65	−2.48	−2.48	−2.53	−2.67	−2.67	−2.58	−2.62	−2.43†	−2.36†	−1.77†

Note. — Concentration index (C_{42}), asymmetry (A), Gini coeffient (G) and normalized second-order moment of the brightest 20% to the total galaxy flux ($\overline{M}_{20}$) at different wavelengths. When the inner radius r_{20} needed to compute C_{42} is smaller than the innermost point in our profiles (or the PSF size, in the case of the 70 μm and 160 μm bands), the quoted values are just lower limits for the actual concentration indices. Values of A, G and $\overline{M}_{20}$ marked with a dagger (†) should be taken with caution, since at the particular distance of each galaxy, the FWHM of the PSF of the affected bands does not allow resolving structures smaller than 0.5 kpc.

Table 9.   Optical recalibration factors.

Galaxy (1)	C_B (2)	C_V (3)	C_R (4)	C_I (5)
NGC 0024	0.947 ± 0.008	1.041 ± 0.013	1.104	2.335 ± 0.011
NGC 0584	0.812 ± 0.006	0.951 ± 0.002	1.150 ± 0.003	1.604 ± 0.019
NGC 0925	0.844 ± 0.101	0.902 ± 0.125	$\cdots$	0.871 ± 0.003
NGC 1097	1.031 ± 0.019	0.970 ± 0.013	1.312 ± 0.017	1.663 ± 0.003
NGC 1291	1.034 ± 0.013	0.943 ± 0.008	1.370	1.738
NGC 1316	1.026 ± 0.009	0.932 ± 0.006	1.247 ± 0.028	1.571 ± 0.010
NGC 1377	2.339 ± 0.154	1.560	2.152	1.825
NGC 1404	1.082 ± 0.012	0.978 ± 0.008	1.272 ± 0.016	1.820 ± 0.013
NGC 1482	0.928 ± 0.100	0.905 ± 0.062	$\cdots$	$\cdots$
NGC 1512	1.109 ± 0.013	1.011 ± 0.017	1.326	2.143 ± 0.008
NGC 1566	1.040 ± 0.022	1.805 ± 0.125	1.895	2.257 ± 0.005
NGC 1705	0.891 ± 0.017	0.933 ± 0.016	1.116 ± 0.099	1.861 ± 0.062
NGC 2798	0.479 ± 0.034	0.642 ± 0.005	$\cdots$	0.960 ± 0.003
NGC 2915	$\cdots$	1.119 ± 0.060	1.246	$\cdots$
IC 2574	0.835	0.855	$\cdots$	$\cdots$
MRK 33	0.344	0.642	$\cdots$	$\cdots$
NGC 3621	0.907 ± 0.139	0.946 ± 0.123	1.658†	0.903
NGC 3773	0.494	0.662	$\cdots$	$\cdots$
NGC 4236	1.015	0.904	$\cdots$	$\cdots$
NGC 4594	0.499 ± 0.012	0.892 ± 0.024	1.297	1.417
NGC 5713	0.823 ± 0.043	0.960	$\cdots$	1.120 ± 0.004
NGC 7331	1.055 ± 0.025	0.941 ± 0.025	1.214 ± 0.034	0.995 ± 0.002
NGC 7552	0.972 ± 0.012	0.971 ± 0.011	$\cdots$	$\cdots$

Note. — Recalibration factors for the SINGS optical data, derived from the compilation of aperture photometry of Prugniel & Heraudeau (1998) (see Appendix A). The fluxes obtained directly from the SINGS images should be multiplied by these factors in order to get values closer to the actual ones. The quoted uncertainties result from the classical statistical formulas for linear fits, and do not include the intrinsic calibration errors of the data from the literature. We estimate that the final recalibrated data carry a global zero-point uncertainty of 10-15%. Missing uncertainties correspond to cases in which there were not enough avalibale data-points to compute the statistical error. Some recalibration factors could not be computed when the aperture photometry catalog did not quote any measured flux for that particular galaxy and band. †The R-band image of NGC 3621 was delivered uncalibrated. This recalibration factor was derived after setting `PHOTFLAM` $= 10^{-7}$ in the FITS header.
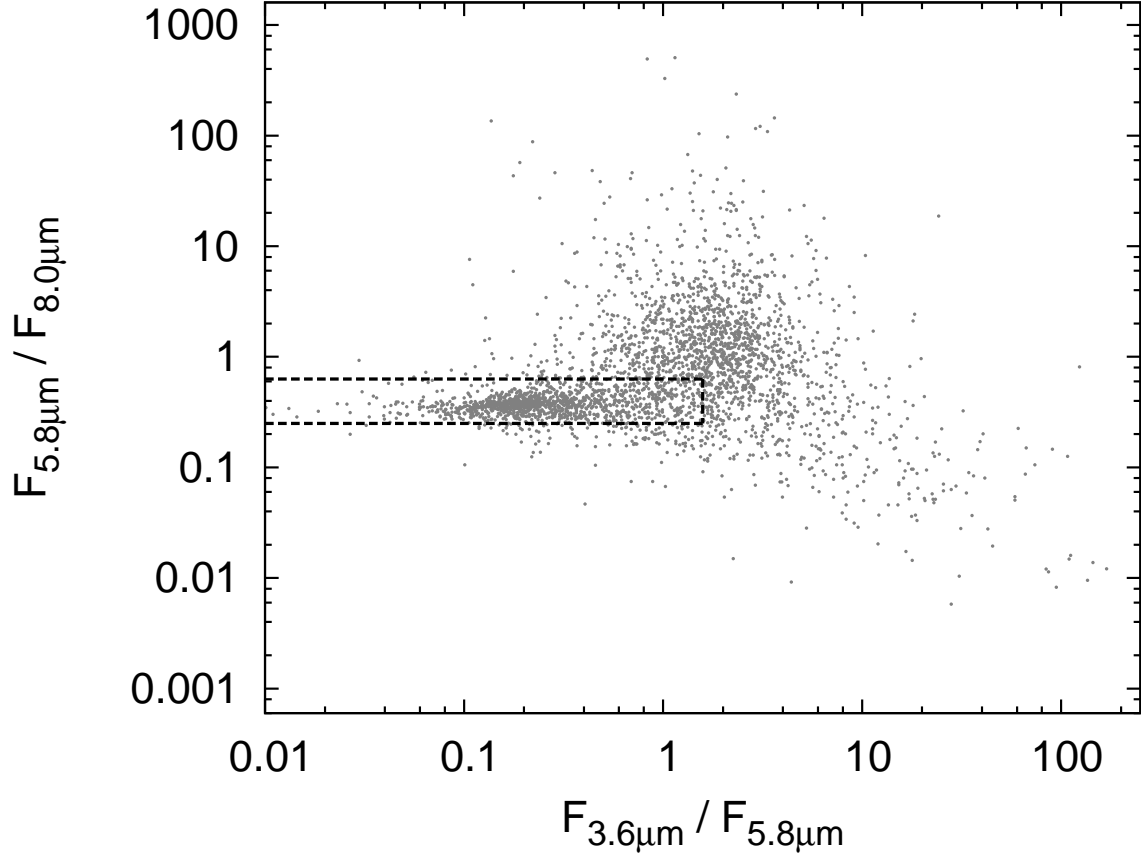
Fig. 1.— IRAC color-color plot of all the diffuse sources detected in the 3.6 μm image of NGC 6946. Star-forming regions within the galaxy are clustered in a thin cloud of points with a roughly constant $(5.8\mu m - 8.0\mu m)$ color. In general, local HII regions of the galaxies in our sample lie within the rectangular region shown with dashed lines. The corresponding colors (see Section 3.1) are used to classify extended objects either as local HII regions or background galaxies. The preliminary masks generated this way are later checked and refined by hand.
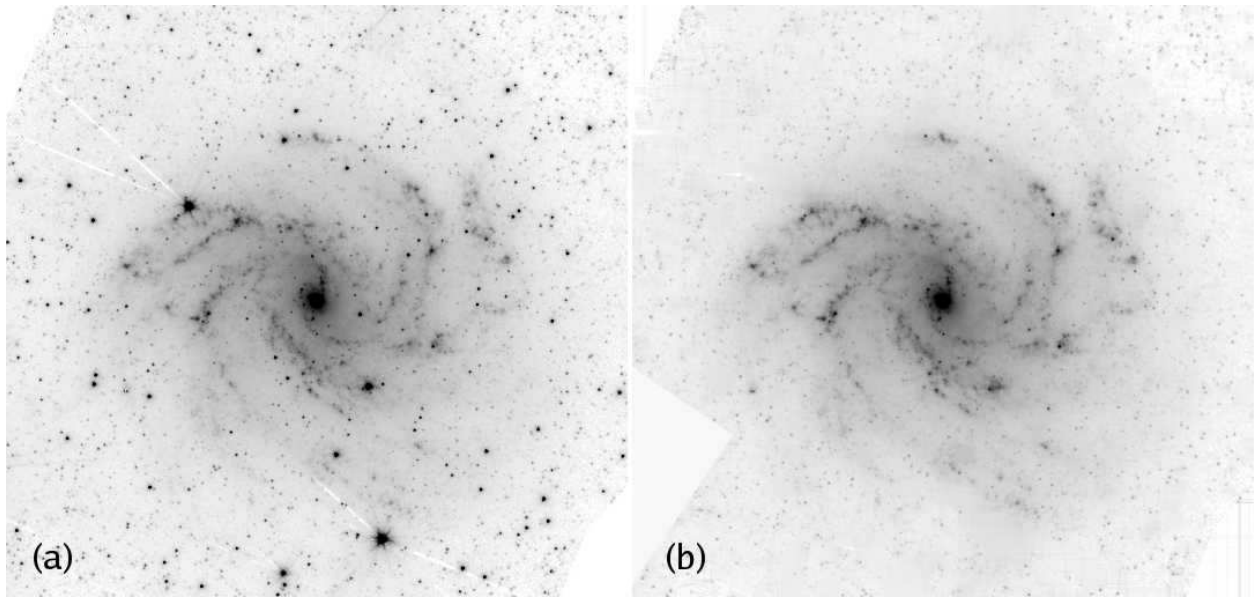
Fig. 2.— (a): Original $3.6\,\mu$m image of NGC 6946. (b): Resulting image after having detected and cleaned foreground stars, background galaxies and artifacts. The same brightness cuts are used to display both images. The diffraction spikes and halo emerging from a very bright star southeast of the galaxy, although barely visible in this printed version of the FITS image, were also masked, hence the blank area in the bottom-left region of the image.
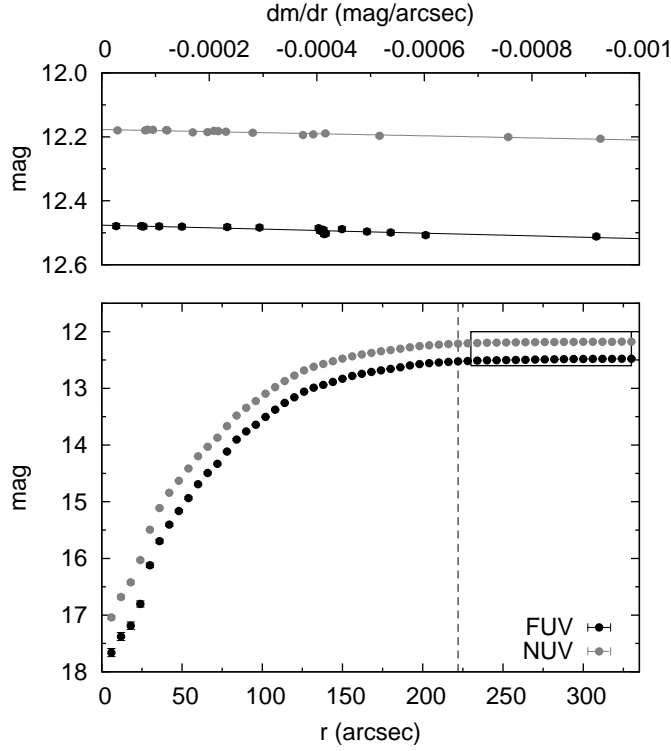
Fig. 3.— Sample plot showing how the asymptotic magnitudes are derived. The bottom panel shows the growth curve of NGC 3184 in the FUV and NUV, that is, the accumulated luminosity inside elliptical apertures with a given radius along the semi-major axis. For comparison, the optical size R25 is shown with a vertical dashed line. For each data-point we compute the radial gradient of the accumulated magnitude, dm/dr, and plot it against the accumulated magnitude itself (top panel). Both quantities usually exhibit a linear behavior in the outer regions of galaxies. The points in the upper panel are those inside the small rectangular box in the lower panel. A linear fit is applied to the data, and the y-intercept (i.e. the accumulated magnitude towards zero-gradient) is taken, by definition, as the asymptotic magnitude.
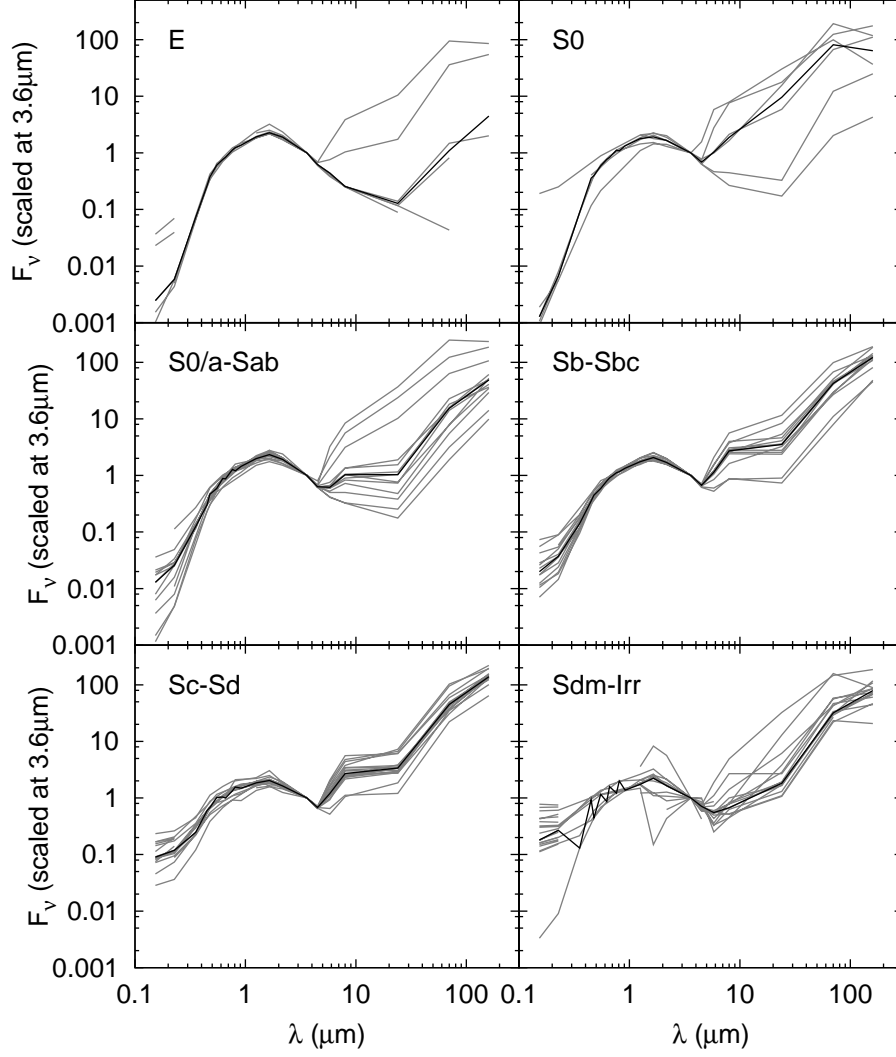
Fig. 4.— Multi-wavelength asymptotic magnitudes of the SINGS galaxies, sorted out into different morphological types. The black solid line indicates the median SEDs in each panel. Small differences between intercalated Johnson-Cousins and Sloan bands can lead to the observed saw-tooth shape in late-type spirals. Note that optical data are missing for some galaxies, when they could not be recalibrated and Sloan data were not available.
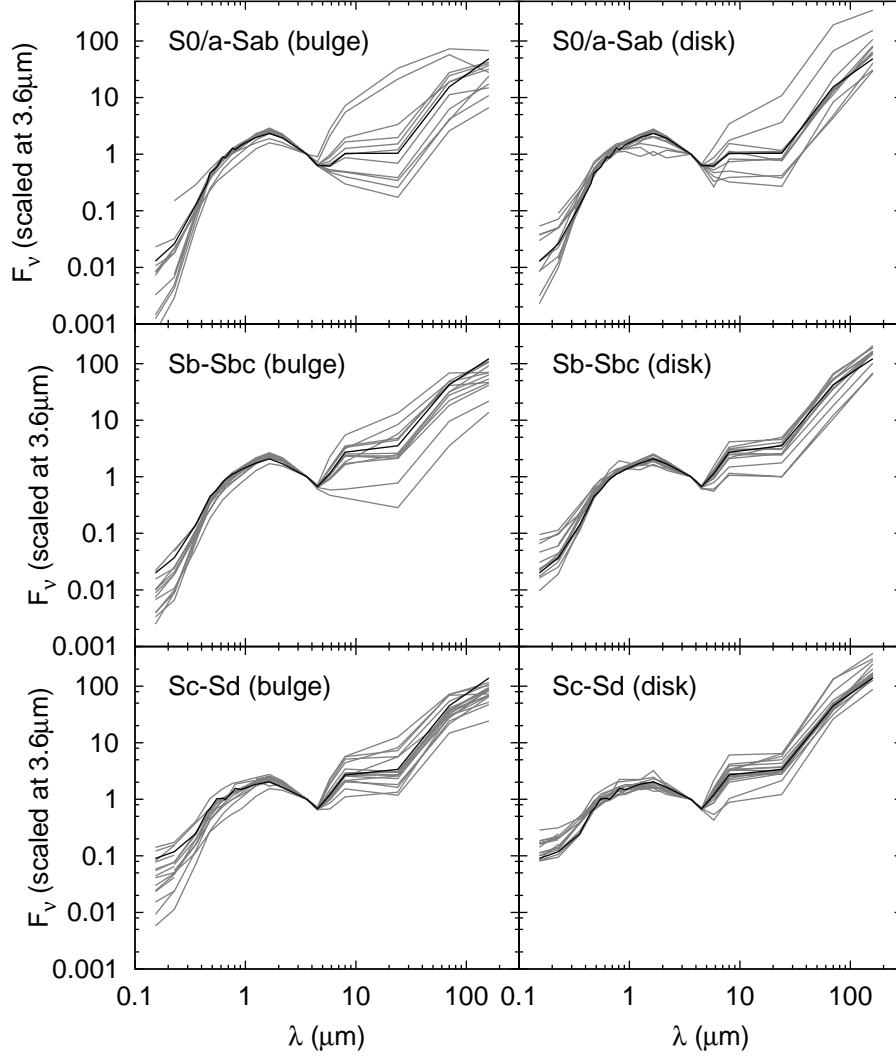
Fig. 5.— Spectral energy distributions of the bulge- and disk-dominated regions of spiral galaxies galaxies. As a reference, the black solid line shows the median SED of galaxies of the corresponding morphological type, taken as a whole (the same curves as those in Fig. 4).
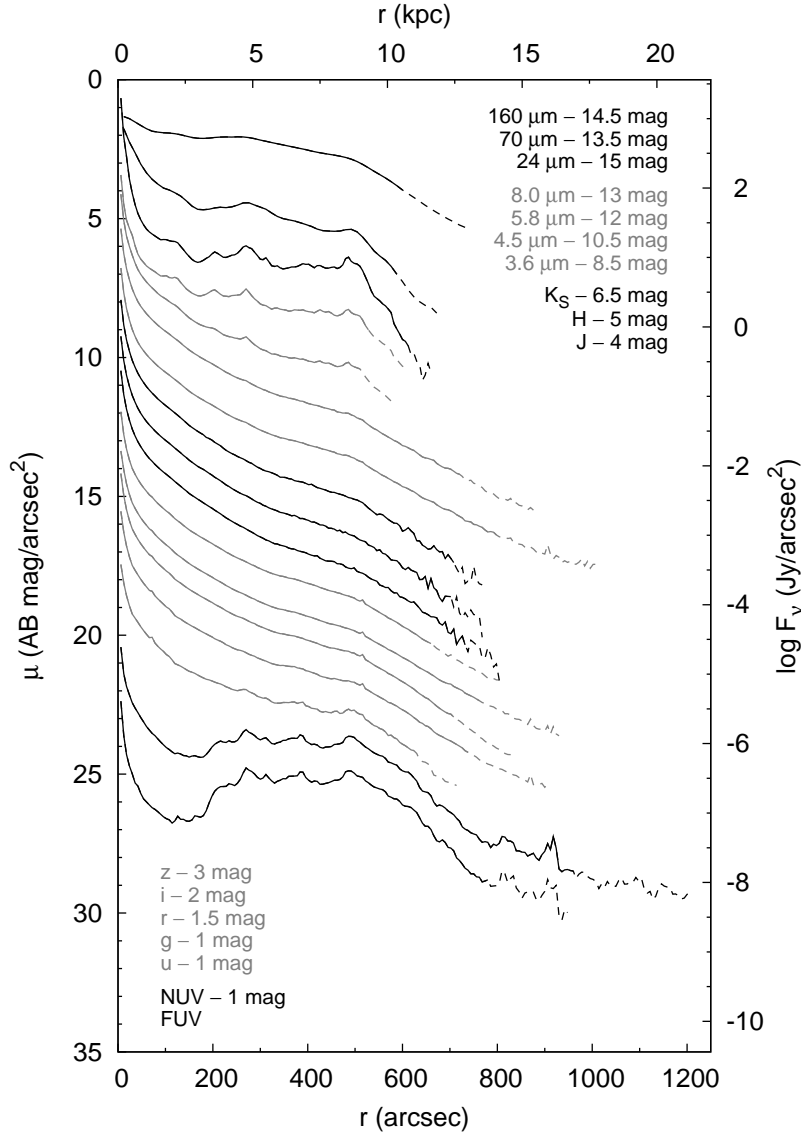
Fig. 6.— Multi-wavelength surface brightness profiles for NGC 3031 (see the on-line edition for the full version of this figure including all galaxies in the sample). The profiles have been shifted for displaying purposes; the corresponding offsets in magnitudes are quoted next to each label. The profiles are arranged in order of decreasing wavelength, from top to bottom, as shown by the labels. For the sake of clarity, black and gray lines are used to group both the profiles and their labels according to their wavelength range (GALEX, optical, 2MASS, IRAC and MIPS, respectively). Errorbars are not shown for clarity (see Tables 2, 3 and 4). The solid profiles have been truncated when $\Delta\mu > 0.3\,$mag, and then continue with dashed lines until $\Delta\mu > 1\,$mag. Note that the large uncertainties in the outermost spatial regions (i.e. those marked with dashed lines) are mostly due to large-scale errors in the background estimation, but do not necessarily imply non-detections. Emission from the galaxy can be clearly seen in these regions above the local noise, although large-scale background variations preclude a more reliable determination of the azimuthally-averaged flux density along these outer isophotes.
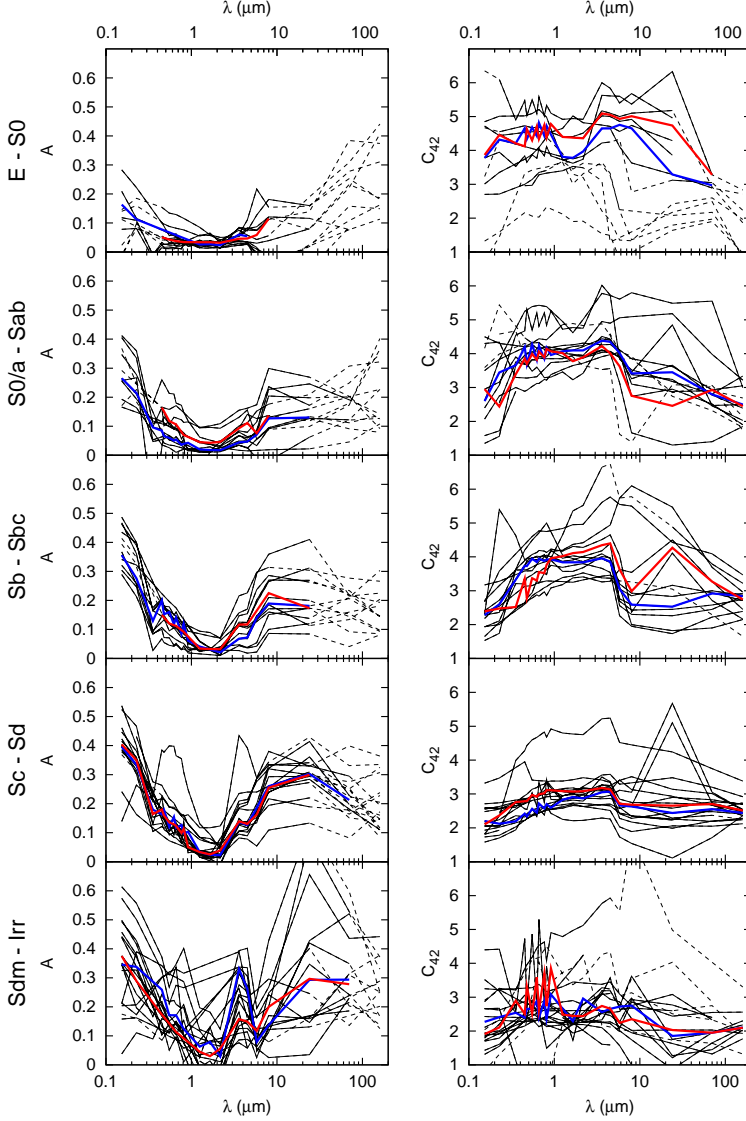
Fig. 7.— Left: Asymmetry of the SINGS galaxies as a function of wavelength, in bins of morphological type. Dashed lines correspond to those bands in which we are unable to resolve structures smaller than 0.5 kpc at the particular distance of each galaxy (note that the meaning of dashed lines is different in the right column, see below). The red (blue) lines show the median values for the galaxies further (closer) than the median distance within each morphological bin (see Section 4.3.1). Dashed lines were not used when computing the red and blue median curves. The galaxy with large optical and infrared asymmetries in the Sc-Sd panel is NGC 5474 (see text). Note that the larger dispersion seen in the Sdm-Irr panel (especially at $3.6\,\mu$m and $4.5\,\mu$m) is probably due to faint unremoved background or foreground sources, since these galaxies have lower surface brightness. Right: Concentration index at different wavelengths. Dashed lines are used when the inner radius r_{20} used to compute C_{42} is smaller than the innermost point of our profiles. These values are then just lower limits. Red and blue lines have the same meaning as in the asymmetry panels.
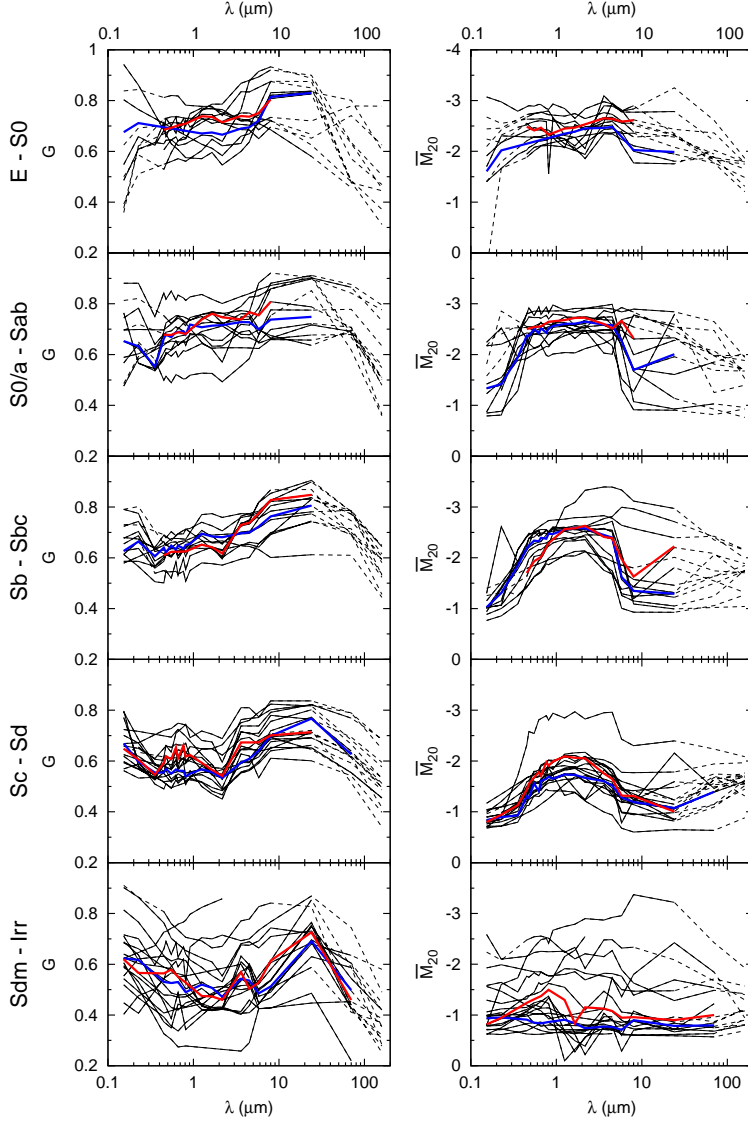
Fig. 8.— Gini coefficient (left) and normalized second-order moment of the brightest 20% of the emission (right) as a function of wavelength and in bins of morphological type. Dashed lines are used when the FWHM in a given band at the particular distance of each galaxy is larger than 0.5 kpc. The red (blue) lines show the median values of the galaxies further (closer) than the median distance within each morphological bin (see Section 4.3.1). Dashed lines were not used when computing these median curves.
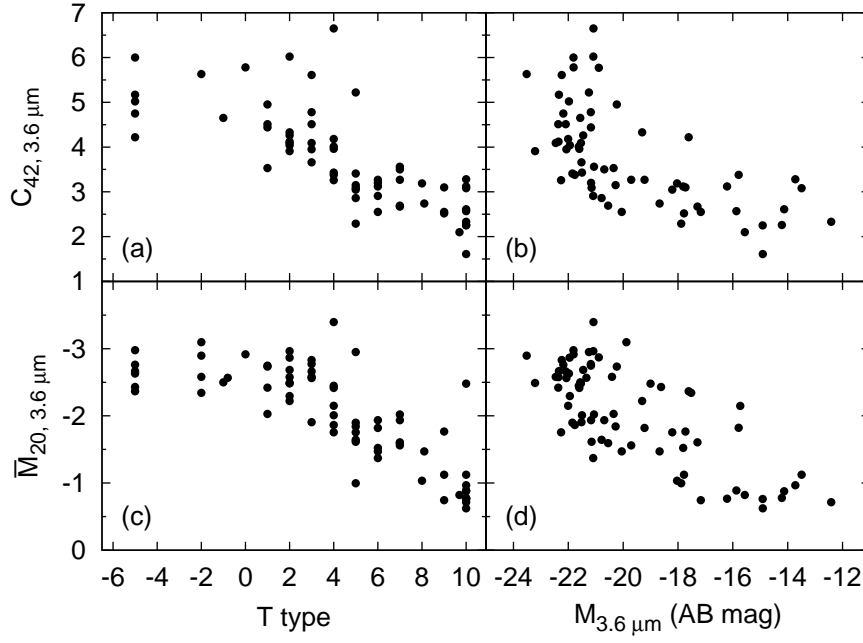
Fig. 9.— Top row: concentration index of the SINGS galaxies at $3.6\,\mu$m as a function of their Hubble type (a) and their absolute magnitude at $3.6\,\mu$m (b). Bottom row: normalized second-order moment of the brightest 20% of the emission as a function of the same quantities.
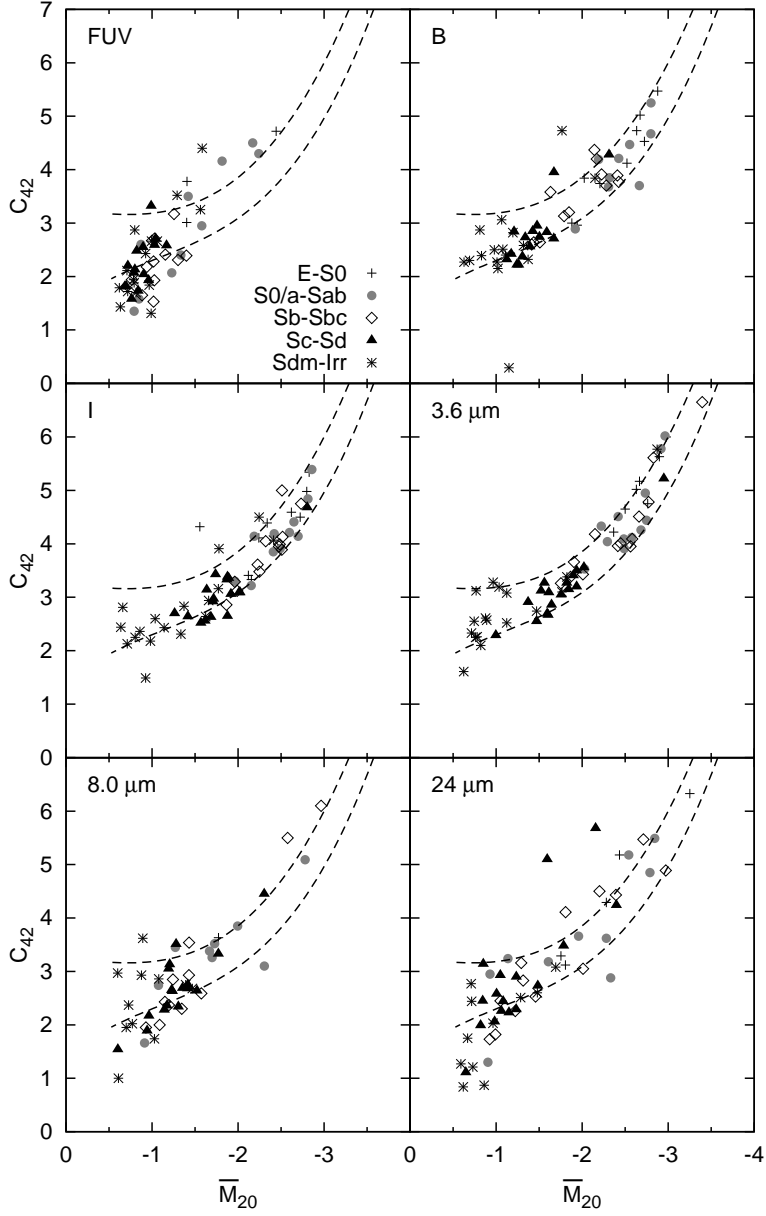
Fig. 10.— Concentration index of the SINGS galaxies as a function of the normalized second-order moment of the brightest 20% of the emission. Trends are shown at selected bands, using different symbols to sort out galaxies into different Hubble types. The dashed lines are third-order polynomials that fit the upper and lower envelopes of the data at $3.6\,\mu$m, and are replicated in all panels to facilitate the visual comparison of the trends at different wavelengths.
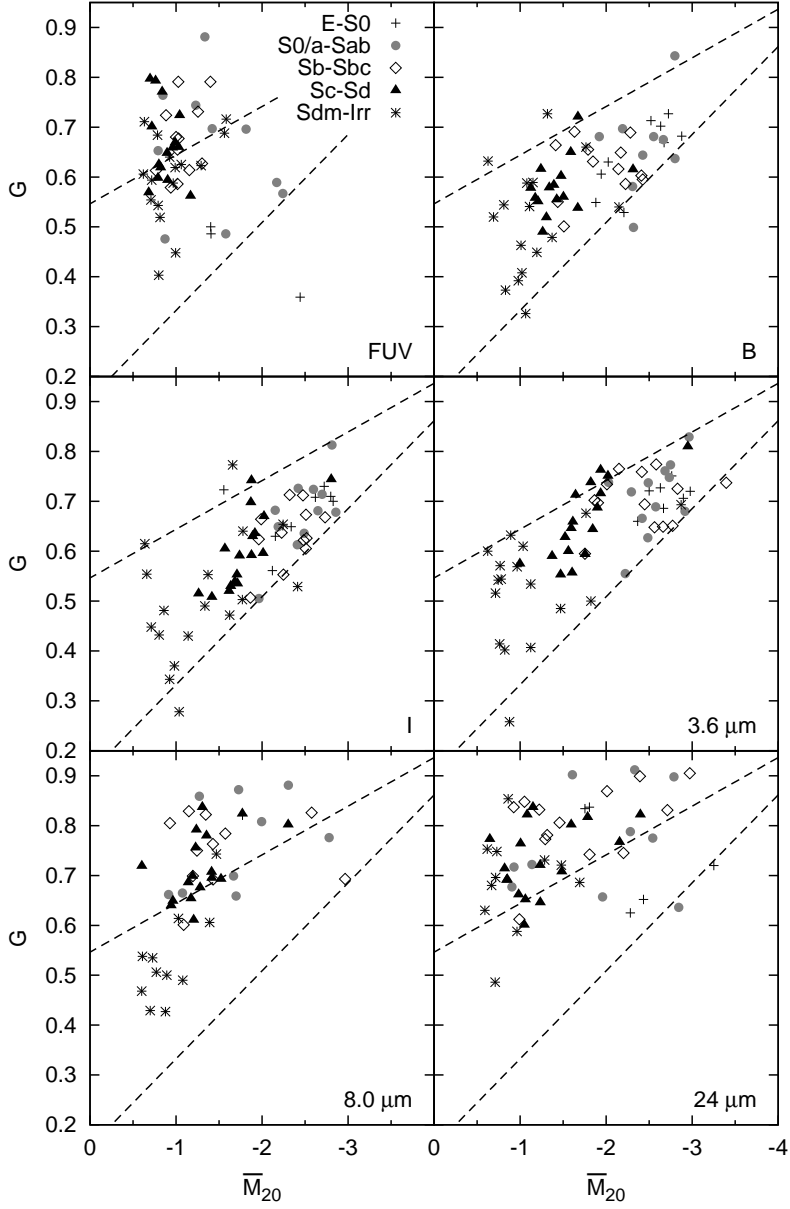
Fig. 11.— Gini coefficient of the SINGS galaxies as a function of the normalized second-order moment of the brightest 20% of the emission. Each panel shows a different band, and Hubble types are coded with different symbols. The upper and lower boundaries of the data-cloud at $3.6\,\mu$m are fitted with two straight lines, which are replicated in all panels for the ease of comparison.
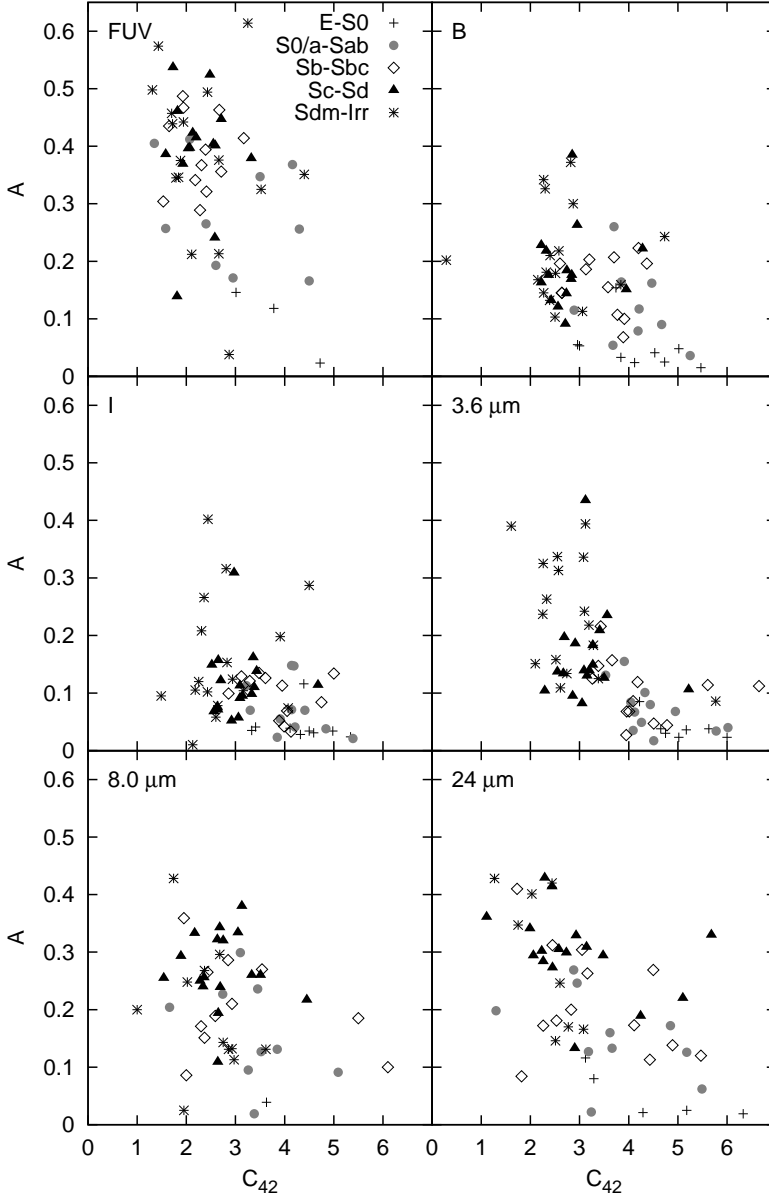
Fig. 12.— Asymmetry of the SINGS galaxies as a function of their concentration indices at several wavelengths. Different symbols are used to sort out galaxies into different Hubble types. Note that, as explained in Section 3.3.2, the systematically large asymmetries displayed by Sdm and irregular galaxies at $3.6\,\mu$m is most probably due to the contribution of foreground and background sources, since galaxies of these Hubble types usually have low surface brightness in the near-IR.
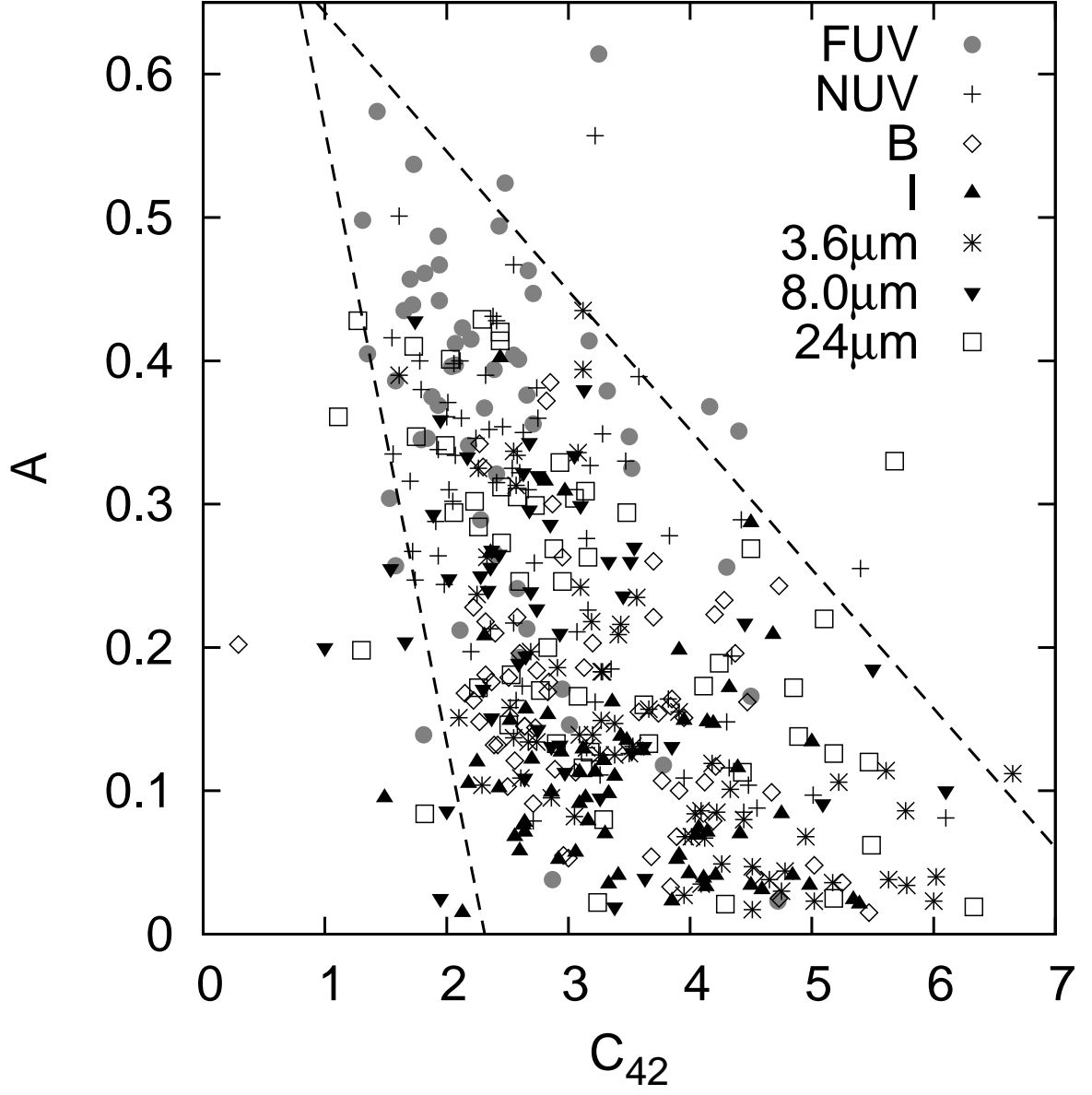
Fig. 13.— Asymmetry as a function of the concentration index for all galaxies and several bands displayed at the same time. The upper and lower limits were obtained by fitting the boundaries of the data-point distribution in all the quoted bands simultaneously.
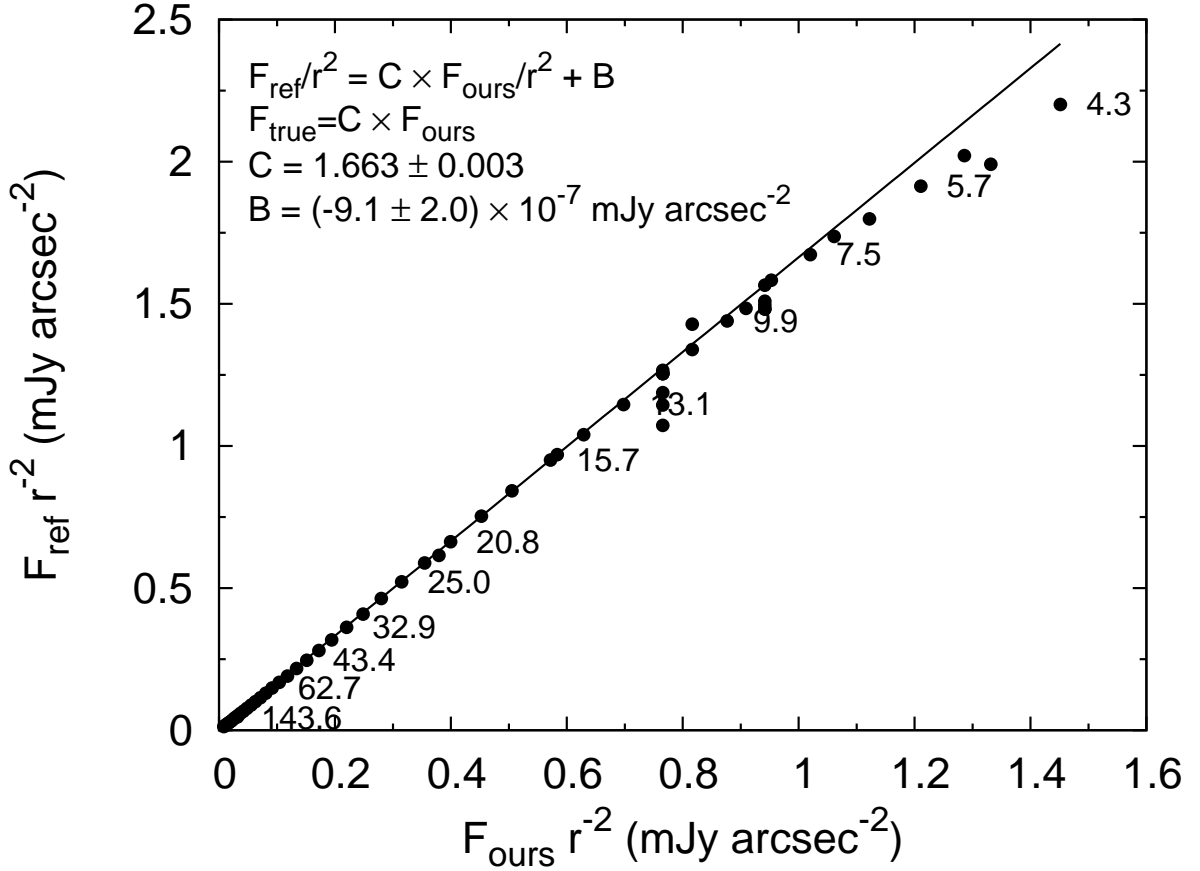
Fig. 14.— Sample recalibration plot for the I-band image of NGC 1097. We compare the flux enclosed inside circular apertures of radius r measured on our images with published aperture photometry (see Appendix A). The small numbers next to each point show the radius in arcseconds of the corresponding aperture (not all of them are shown for clarity). Very small apertures do not always follow the linear trend, likely due to differences in the PSF and centering errors, and are thus excluded from the fitting.